Stony Brook University

High-Order Adaptive Extended Stencil Finite Element Methods for Applications with Curved Boundaries

A Dissertation presented

by

Tristan Joseph Delaney

to

The Graduate School

in Partial Fulfillment of the

Requirements

for the Degree of

Doctor of Philosophy

in

Applied Mathematics and Statistics

Computational Applied Mathematics

Stony Brook University

May 2017

Stony Brook University

The Graduate School

Tristan Joseph Delaney

We, the dissertation committee for the above candidate for the

Doctor of Philosophy degree, hereby recommend

acceptance of this dissertation

Xiangmin Jiao - Advisor
Associate Professor, Department of Applied Mathematics and Statistics

James Glimm - Chairperson of Defense
Distinguished Professor, Department of Applied Mathematics and Statistics

Roman Samulyak
Professor, Department of Applied Mathematics and Statistics

Shikui Chen
Assistant Professor, Department of Mechanical Engineering

This dissertation is accepted by the Graduate School

Charles Taber
Dean of the Graduate School

Abstract of the Dissertation

High-Order Adaptive Extended Stencil Finite Element Methods for Applications with Curved Boundaries

by

Tristan Joseph Delaney

Doctor of Philosophy

in

Applied Mathematics and Statistics

Computational Applied Mathematics

Stony Brook University

2017

High-order numerical methods for PDE discretizations have attracted significant interests for scientific and engineering applications in recent years. For engineering problems with complex geometries, achieving high-order convergence is decidedly challenging, especially with curved boundaries. The existing high-order finite element methods based on isoparametric elements require the definition of curved volumetric elements to represent the geometry accurately and ensure the validity of their variational formulations. However, these high-order elements have much stricter mesh quality requirements due to the possibilities of internal foldings of the elements, which are very hard to detect. In addition, poor mesh quality may also lead to potential loss of the completeness of the basis functions. Some recently proposed alternatives such as isogeometric analysis and NURBS-enhanced FEM can achieve high-order convergence but are very complicated and also have even stricter requirement on mesh quality.

In our recent work, we have developed the adaptive extended stencil fi-

nite element method (AES-FEM), which has less dependent on mesh quality. In this dissertation, we extend the AES-FEM to achieve high order convergence on geometries with curved boundaries and Neumann boundary conditions. AES-FEM uses high-degree polynomial basis functions to accurately discretize the PDE. In the interior, AES-FEM uses piecewise linear test functions for simplicity and efficiency. For elements adjacent to the curved boundary, we construct new superparametric elements, whose test functions are piecewise linear in the parametric space but curved in the real space to capture the curved geometry accurately. We construct these superparametric elements using simplices with curved faces and edges defined by the curved geometry.

As another contribution, we propose a new strategy for enforcing Neumann boundary conditions for weighted residual methods in the variational formulations, which only require integrating the Neumann boundary conditions over small regions on the boundary. The method is consistent with the variational problem and simplifies some of the implementation, and it allows enforcing Neumann boundary conditions even for boundaries with discontinuous normal directions. We present the method both for AES-FEM as well as generalized finite difference (GFD) methods. We present results of our method applied to second-order elliptic problems on curved boundaries.

Dedication Page

This dissertation is dedicated to my parents who have always supported me throughout my journey.

Contents

Acronyms

AES-FEM adaptive extended stencil finite element method

DEM diffuse element method

DGFEM discontinuous Galerkin finite element method

EFG element-free Galerkin method

FDM finite difference method

FEM finite element method

FVM finite volume method

GFD generalized finite difference

GLPBF generalized Lagrange polynomial basis function

IGA isogeometric analysis

MWR method of weighted residual

NEFEM NURBS-enhanced finite element method

NURBS non-uniform rational B-splines

PDE partial differential equation

WALF weighted average of least squares fittings

List of Tables

List of Figures

Acknowledgements

I would like to acknowledge the help and support of my advisor, Professor Xiangmin Jiao. Many thanks go out to my colleagues at the Applied Mathematics and Statistics Department including the NumGeom group and at the IACS. Special thanks to my collaborators Professor Rebecca Conley, Dr. Cao Lu, Dr. Verinder Rana, Dr. Navamita Ray, Dr. Hongxu Liu, Dr. Xinglin Zhao, Wei Li, and Professor Roman Samulyak with whom I had years of interesting discussions and collaboration. I would also like to thank Aditi Ghai and Xuebin Wang for their support.

I would also like to extend a warm thank you to my colleagues at the Institute for Advanced Computational Science. It is a wonderful institute with diverse and fascinating research opportunities. Lastly, I would like to thank all of my family and friends who have supported me through my time in graduate school.

Chapter 1

Introduction

The success of the finite element method (FEM) has been due to the need of engineers, scientists, and mathematicians to handle ever increasingly large-scale physical problems involving complex geometries, multiphysics, and multiple types of boundary conditions. Finite element software is ubiquitous in the automobile, aerospace, and shipbuilding industries and makes up a multi-billion dollar market [32]. Finite elements have driven the research and development of advanced meshing techniques to discretize complex geometries, in particular because the representation of geometry is closely tied to the relationship of the mesh. Indeed, *isoparametric* elements use the same functions to represent the geometry as they do the actual finite element function space used to discretize the partial differential equation (PDE) [10, 14].

The requirements of FEMs as well as finite volume methods (FVMs) and finite difference methods (FDMs), have motivated decades worth of re-

search for computational geometers and applied mathematicians into what exactly a "good *mesh quality*" is. This question has its roots in geometric interpretations of the linear test functions over simplices in the context of interpolation error over refinements of meshes. Zlámal suggested the minimum angle among triangles should be bounded below by a constant [75], while the seminal paper [1] showed that the maximum angle condition was "essential" for the convergence of FEM. However these conditions are only made in the asymptotic context of sequences of triangulation refinements. Additional measures of for meshes with moderate quality have been proposed in [62] for linear triangles and tetrahedra which bound the interpolation errors in terms of various geometric properties of triangles. Algebraic mesh quality measures have also been suggested which also apply to other element topologies such as quadrilaterals or hexahedral meshes [41].

For problems with curved boundaries, it becomes necessary to represent the boundary to high order in order for FEM to converge to high-order[3]. This creates additional challenges for the meshing community as mesh optimization becomes more difficult. Oftentimes, the geometry is represented through a parametric mapping from some reference element to each of the mesh elements. If the Jacobian of this parametric mapping is negative, then the parametric mapping is no longer a homeomorphism; and if the Jacobian is nearly singular at some points then the condition number of the resulting linear system may become very large. Detecting these poor quality elements is expensive and requires costly optimization procedures [16, 38, 40]. Often-

times, poor quality elements exist near boundary features where large aspect ratios and complex features make it difficult for parametric elements to be created from standard linear mesh generation techniques.

The adaptive extended stencil finite element method (AES-FEM) was designed to overcome difficulties with mesh quality while still preserving the advantages that meshes provide. It has been successfully shown to handle linear meshes with poor quality [19], as well as having the ability to obtain high-order accuracy from only a linear mesh [18]. In particular, it achieves this by constructing new basis functions from a *weighted least-squares* (WLS) approximation in contrast to the more typical interpolatory techniques used in traditional finite elements. This provides robustness by replacing the approximation of the function by a stencil of neighboring vertices rather than defining a set of basis functions over individual elements. Additionally, the mesh provides a simple data structure for determining vertices to include inside each stencil as well as domains for numerical integration to be performed. In the previous work, this has been done solely on linear meshes for PDEs with pure Dirichlet boundary conditions.

This dissertation expands upon the work that was presented in [19] and [18] in three areas. First, we introduce how to generate new test functions for AES-FEM using *superparametric* elements generated from the curved boundary. In particular, issues regarding guaranteeing of well-defined parametric mappings are discussed. Second, the issue of interpolating Neumann boundary conditions from linear meshes is considered and the issues pertaining to

high-order numerical integration over surfaces are discussed. Lastly, a novel implementation of Neumann boundary conditions is proposed for AES-FEM and, more generally, *methods of weighted residuals* (MWRs) where the appropriate test functions are defined only on the surface. We use this new boundary treatment in the contexts of AES-FEM and generalized finite difference (GFD) methods.

This dissertation is less of a discussion of mesh quality measures as it is a fundamental retreatment of geometry with PDEs. AES-FEM had been used in [19] to overcome issues of mesh quality while restraining itself to quadratic basis functions on simplicial meshes, and it was generalized to high-order polynomial basis functions defined on simplicial meshes in [18]. In this dissertation, we add new functionality to AES-FEM, specifically Neumann boundary conditions and special treatment of curved boundaries.

For problems with curved boundaries, Neumann boundary conditions become more challenging as the test functions no longer decay to zero and geometric errors begin to dominate over truncation and integration errors. In particular, the basis functions in AES-FEM are merely polynomials without compact support, and the geometry is represented by the test functions, which are chosen to be finite element shape functions constructed from the mesh itself. Therefore, it becomes necessary to define new test functions which can accurately represent the geometry to high-order, while maintaining the order of consistency from the basis functions.

The remainder of this dissertation is outlined as follows: Chapter 2 cov-

ers a brief outline of the current state of finite element methods. Chapter 3 provides the background and basic implementation of AES-FEM including the generalized Lagrange polynomial basis functions. Chapter 4 discusses the treatment of curved boundary conditions and Neumann boundary conditions in AES-FEM. Chapter 5 introduces a new variational formulation for the treatment of Neumann boundary conditions using boundary integrals. Chapter 6 applies our proposed methods for several second-order elliptic problems on curved geometries. Finally Chapter 7 offers concluding remarks and directions for further research.

Chapter 2

Background and Related Work

Let $\Omega \subset \mathbb{R}^d$ be a bounded domain with boundary $\partial\Omega = \Gamma_D \cup \Gamma_N$. Let $\mathcal{L}$ be a second order elliptic linear differential operator

$$\mathcal{L} = \sum_{1 \leq i,j \leq d} -\frac{\partial}{\partial x_i}\left(a_{ij}\left(\boldsymbol{x}\right)\frac{\partial}{\partial x_j}\right) + \sum_{1 \leq i \leq d} b_i\left(\boldsymbol{x}\right)\frac{\partial}{\partial x_i} + c\left(\boldsymbol{x}\right). \tag{2.1}$$

The associated boundary value problem is to find a sufficiently smooth solution $u \in C^2\left(\Omega\right) \cap C^1\left(\overline{\Omega}\right)$ such that

$$\mathcal{L}u = f, \qquad \text{on } \Omega. \tag{2.2}$$

The solution u may have to satisfy some boundary conditions on the boundary of the domain, $\partial\Omega$. These boundary conditions may be Dirichlet (otherwise known as *essential*) or Neumann (otherwise known as *natural*) boundary

conditions

$$u = \bar{u}, \text{on } \Gamma_D, \tag{2.3}$$

$$\frac{\partial u}{\partial n} = g, \text{on } \Gamma_N. \tag{2.4}$$

The most general means of approximating the solution to (2.2) is through the method of weighted residual (MWR) [24]. In MWR, the solution u is expanded as a linear combination of *basis functions* $u = \sum_{j=1}^{N} u_j \phi_j$, where $u_j \in \mathbb{R}$ denote the coefficients of the linear combination. The basis functions must satisfy the essential boundary conditions (2.3) while the natural boundary conditions (2.4) are enforced automatically. The residual of a point $\boldsymbol{x} \in \Omega$ is

$$R(u, f) := \mathcal{L}u - f,$$

and the *weighted residual* is

$$(R, v) = \int_{\Omega} Rv \, \mathrm{d}\Omega,$$

where v is an appropriate *test function*. MWR uses a set of test functions v_i such that

$$\int_{\Omega} R\,(u, f)\, v_i \, \mathrm{d}\Omega = 0, \qquad \text{for } i = 1, \ldots, N. \tag{2.5}$$

This results in a system of linear equations for linear PDEs.

The different choices for both basis functions ϕ_j and test functions v_i lead to a variety of numerical methods, and each method may have advantages

Property	Basis Functions	Test Functions
Completeness	Yes	Optional
Compact Support	Optional	Yes
Integrability	Yes	Yes
Lagrange Property	Preferred	No

Table 2.1: List of basic properties of MWR.

over the others. For example, the basis functions must generally form a complete basis in the sense that any polynomial up to some degree d must be reproduced exactly. The test functions, on the other hand, are often desired to have compact support and some level of smoothness. Table 2.1 summarizes many of the desired properties of both the test and basis functions. In the following sections, we provide a brief description of these methods, their benefits, and their challenges.

2.1 Galerkin Methods

Galerkin methods choose the basis functions to be equal to the test functions in (2.5). Specifically, the finite element method uses basis functions that are piecewise polynomials defined over individual mesh elements; these functions are also used in computing the derivatives and integrals. FEMs typically solve (2.5) by performing integration by parts and substituting any natural boundary conditions (2.4) specified by the problem. For test functions that

satisfy $v|_{\partial\Omega_D} = 0$, integration by parts allows for (2.5) to be rewritten as

$$a(u, v) = F(v), \tag{2.6}$$

where

$$\begin{aligned} a(u, v) = &\int_\Omega a_{ij} \frac{\partial u}{\partial x_j} \frac{\partial v}{\partial x_i} \, \mathrm{d}\Omega \\ &+ \int_\Omega b_i \frac{\partial u}{\partial x_i} v \, \mathrm{d}\Omega \\ &+ \int_\Omega cuv \, \mathrm{d}\Omega \end{aligned} \tag{2.7}$$

$$F(v) = \int_\Omega fv \, \mathrm{d}\Omega + \int_{\Gamma_N} gv \, \mathrm{d}\Gamma. \tag{2.8}$$

Equation (2.7) has the advantage that it only requires the the first partial derivatives of the function u, which significantly lessens the burden of discretizing the function space.

Let $\{\phi_i\}_{i=1}^N$ be a basis for a finite dimensional vector space V_h, then a linear system of equations is formed with

$$\begin{aligned} \boldsymbol{A}\boldsymbol{x} &= \boldsymbol{b} \\ A_{ij} &= a(\phi_j, \phi_i) \\ b_i &= F(\phi_i). \end{aligned}$$

The matrix $\boldsymbol{A}$ is often referred to as the *stiffness matrix* while the vector $\boldsymbol{b}$ is the *load vector*. These names are derived from solid mechanics where

the stiffness matrix represents the internal forces present in the solid material, which resist the external loads experienced by the material. For many classes of elliptic boundary problems, the resulting linear system is sparse, symmetric, and positive-definite (SPD). This has the benefit of being able to use simple sparse linear solvers such as preconditioned conjugate gradient method (PCG).

Central to the computation of the stiffness matrix and load vector is the discretization of both the function space and the geometry of the domain Ω. Traditionally, this is achieved through the use of a simplicial meshes where the domain is discretized into separate triangles or tetrahedra in two or three dimensions, respectively. Let $\mathcal{T}$ be a triangulation of Ω so that the domain $\Omega \approx \Omega_h = \bigcup_i K_i$, where K_i are individual triangular or tetrahedral elements of the mesh. In the assembly of the stiffness matrix and load vector, integration over the domain is split into seperate integrals over each individual element.

Integration over each element is performed by defining quadrature rules over a *reference element*, $\tilde{K}$, using a parametric mapping from $\Phi : \tilde{K} \rightarrow K$. Although this parametric mapping is flexible, it can also be a source of instability as any elements with large or small angles tend to lead to large condition numbers [1, 62, 75]. For linear meshes, there are a variety of estimates of *mesh quality*, which are used to quantify how well the FEM may be expected to perform on certain meshes. These mesh quality measures are often based on estimates of the interpolation of smooth functions to the

Jacobian of the transformation Φ. Even for linear meshes, it is difficult to guarantee "good" mesh quality in three dimensional tetrahedral meshes due to the existence of slivers [64] or poor quality elements near complex features. In [19], it was shown that even a small number of bad quality elements can lead to drastic change in the condition number of the matrix and the number of iterations in the linear solver.

For problems with curved geometries, linear meshes may inadequately represent the geometry and constrain the performance of finite element solvers to second order [3]. In particular, this necessitates the high-order representation of the geometry itself through the generation of *curved* elements. Let K be an element of a mesh with k basis functions. Any function may be written in terms of the m basis functions are defined and the solution $u|_K$ can be expressed as

$$u_h|_K = \sum_{i=1}^{k} u_i \phi_i \left(\boldsymbol{x} \right), \quad \boldsymbol{x} \in K.$$

Oftentimes, the basis functions may be Lagrange polynomials, but they may also be chosen to be classes of orthogonal polynomials such as Legendre or Chebyshev. The integration over the element K requires the parameterization of K in terms of a set of *shape functions* of the finite element, which represent the geometric mapping from the reference element to the physical element. Shape functions are a set of functions ϕ_j^*, usually polynomials, such

that

$$\boldsymbol{x}|_K = \sum_{i=1}^{m} \boldsymbol{x}_i \phi_i^* (\boldsymbol{x}) .$$

Isoparametric elements correspond to the case where $m = k$ and $\phi_i = \phi_i^*$. For $m > k$ (resp. $m < k$), then the element is said to be *superparametric* (resp. *subparametric*). Typically, the classical isoparametric formulation constructs elements using Lagrange polynomials to represent both the basis/test functions as well as the geometry [14]. The computation of integrals can still be done over a reference element, but the basis functions will no longer be polynomials [10]. These isoparametric finite element methods have much stricter mesh quality requirements due to the possibility of inversion or near singular Jacobians of the isoparametric transformation. Thus, these high order meshes require mesh optimization procedures to ensure that local isoparametric representations of the geometry are in fact diffeomorphic to the reference or some ideal element [27, 39, 41, 51, 56, 57].

2.2 Meshless Methods

Meshless methods are a general class of numerical discretizations which focus on point-cloud descriptions of the domain without reference to any volumetric "elements" [2, 6]. Meshless methods such as smooth particle hydrodynamics (SPH) [30, 47] use the concept of kernel functions to achieve compact support as well as numerical approximation of the derivatives of the PDE. These kernel functions generally have requirements of partition of unity and

smoothness to ensure consistency of the numerical approximation, and several choices including truncated Gaussian distributions [30], splines [6], and radial basis functions [11]. Central to these methods is the domain of influence and the choice of numerical quadrature rules, which may complicate the implementation [6]. The stability of the meshless methods has been shown to be determined by the *completeness* of the kernel, that is the ability of the kernel functions to approximate polynomials up to a certain degree; and the *integrability* of the kernel functions [5]. If these conditions are not satisfied, then the methods may fail to converge.

Another class of meshless methods were introduced with the diffuse element method (DEM) [49] and further developed with element-free Galerkin method (EFG) [7]. For both of these methods, the domain is represented as a point cloud with some description of the domain. Basis functions are constructed using a moving least-squares approximation (MLA) [42] to estimate derivatives. Integration is performed on quadrature rules for Cartesian grids with essential boundary conditions being enforced weakly using Lagrange multipliers. DEM and EFG are Galerkin methods, which use the MLA basis functions as polynomials. Central to compactness of these methods is the use of a weighting function that restricts the domain of influence of each node in the point cloud. These methods do not have the issue of poor mesh quality, but can still suffer from poor selections of local neighrhoods and difficult choices of numerical integration rules.

2.3 CAD-Enhanced Galerkin Methods and Isogeometric Analysis

Others like isogeometric analysis (IGA) [32, 20, 4] and NURBS-enhanced finite element method (NEFEM) [59, 60] incorporate the exact geometry of a CAD model into the finite element discretization. These methods have gained much popularity over the past decade as CAD models are integral in the design process for many industries.

Isogeometric analysis directly constructs basis and test functions from the CAD model's NURBS [32] or T-splines [4] representation of the entire volume of the domain. It ties the use of the splines and the exact representation of the geometry together with the discretization of the solution function space. The individual splines provide both smoothness and compact support necessary for Galerkin methods. Condition number estimates for IGA were shown to be similar to those of traditional FEMs in [26]. IGA has been applied successfully in several settings for boundary value and time-dependent problems [21, 73]. Issues of *model quality* have been increasingly researched over the past several years to estimate *a priori* the performance of IGA from properties of the CAD model [17]. Severe distortions of control points often require may also cause a loss of consistency for low degree NURBS [44], and the modeling of fine structures such as fillets requires special care on the part of the modeler.

In contrast, NEFEM constructs curved elements using the NURBS rep-

resentation only one the surface of the boundary while maintaining traditional isoparametric elements within the interior [59, 60]. NEFEM only requires the special treatment of elements with at least one edge or face on the non-uniform rational B-splines (NURBS) boundary. The elements are constructed by assigning new parametric mappings between a referential prism element that blend the NURBS surface into the interior vertices. Basis functions and test functions can be constructed from Lagrange polynomials either in the parametric space for continuous Galerkin approximations or in the physical space for discontinuous Galerkin approximations.

2.4 Finite Difference Methods and Their Generalizations

A broad but important class of numerical methods for PDE discretization are the finite difference (FDM) and finite volume (FVM) methods. Finite difference methods are among the oldest numerical methods for solving PDEs, although they have fallen out of favor with engineers due to their perceived difficulties in using complex geometries. Finite difference methods use Dirac delta functions as the weight functions in (2.5) and construct local polynomial approximations of the function and its partial derivatives at the vertices of the mesh [8, 25, 28, 43, 50, 67]. Function values away from the mesh vertices are generally not considered. Finite difference methods do not have a concept of mesh quality, but do rely on judicious selection of local *stencils* to

make the resulting differentiation rules stable [34, 33, 45]. In *classical* finite difference methods, stencils are taken from a global Cartesian grid which leads to well known finite difference formulas for various partial derivatives. However because of the nature of Cartesian grids, it is difficult to use these methods on complex geometries.

Numerous generalizations of FDMs have been investigated in the past. Many of these [46, 48, 58] rely on a local least squares approximation from a set of basis functions to approximate derivatives at the vertices including radial basis functions [11, 63, 72] and weigthed least squares approximation of local polynomial basis functions [8, 43, 46, 48, 50, 52]. In particular methods that use latter choice of basis functions, known as generalized finite difference methods (GFDMs), can be used on unstructured meshes of complex and dynamically changing geometries. These include problems with heat transfer over complex or irregular geometries [13], estimations of geometric quantities of surfaces [16, 37, 70, 71], and and mesh smoothing via geometric flows [15]. GFDMs are capable of modeling a wide range of applications including fluid dynamics [9] and solid mechanics [46, 48, 69].

Chapter 3

Adaptive Extended Stencil Finite Element Method

The adaptive extended stencil finite element method was developed for problems involving meshes that may have less than perfect element quality. The idea of AES-FEM is simple: combine the robustness of weighted least-squares approximation with the ease of integration and natural enforcement of boundary conditions provided by the finite element test functions of a mesh. AES-FEM constructs a its basis functions from generalized Lagrange polynomial basis functions (GLPBFs), which are derived from a local WLS approximation. The GLPBFs are consistent up to high order and can be adapted as needed for the solution of (2.6). We discuss the derivation and basic properties of the GLPBFs and their inclusion in AES-FEM.

3.1 Generalized Lagrange Polynomial Basis Functions

Consider any vertex $\boldsymbol{x}_k$ on a mesh or point cloud. Any collection of $m+1$ vertices $\{\boldsymbol{x}_0, \boldsymbol{x}_1, ..., \boldsymbol{x}_m\}$ with $\boldsymbol{x}_0 = \boldsymbol{x}_k$ is called a stencil *of the vertex* $\boldsymbol{x}_k$ with radius $h = \max_{0\leq i\leq m}\{\|\boldsymbol{x}_i - \boldsymbol{x}_0\|\}$. Let $\delta\boldsymbol{x}_i = \boldsymbol{x}_i - \boldsymbol{x}_0$. Then any function $u(\boldsymbol{x}) = u(\boldsymbol{x}_0 + \delta\boldsymbol{x})$ may be approximated at the individual points $\boldsymbol{x}_i = (x_i, y_i)$ by a degree p Taylor series expansion

$$u(\boldsymbol{x}_i) = \sum_{d=0}^{p} \sum_{r\geq 0, s\geq 0}^{r+s=d} c_{rs}\delta x_i^r \delta y_i^s + O\left(h^{p+1}\right). \tag{3.1}$$

We may equivalently write the equation above as

$$u(\boldsymbol{x}_i) = \boldsymbol{c}^T \boldsymbol{\mathcal{M}}(\delta\boldsymbol{x}_i) + O\left(h^{d+1}\right) \tag{3.2}$$

where

$$\boldsymbol{c} = \left[c_{00}\ c_{10}\ c_{01}\ c_{20}\ c_{11}\ c_{02}\right]^T,$$
$$\boldsymbol{\mathcal{M}}(\delta\boldsymbol{x}) = \left[1\ \delta x\ \delta y\ \delta x^2\ \delta x\delta y\ \delta y^2\right]^T$$

are the vector of polynomial coefficients and the monomial basis, respectively, for $p = 2$.

Considering (3.1) for each of the $m+1$ vertices in the stencil results in

the system of linear equations

$$\boldsymbol{V}\boldsymbol{c} \approx \boldsymbol{b}, \tag{3.3}$$

where $b_i \equiv u(\boldsymbol{x}_i)$. The matrix $\boldsymbol{V}$ is the Vandermonde matrix of the stencil $\boldsymbol{X}$. The least square problem is then to find a solution of polynomial coefficients $\boldsymbol{c}$ which minimizes the least-squares error of (3.3), that is

$$\boldsymbol{c} = \arg\min_{\boldsymbol{x}\in\mathbb{R}^n} \|\boldsymbol{V}\boldsymbol{x} - \boldsymbol{b}\|_2^2. \tag{3.4}$$

If $\boldsymbol{V}$ is of full column rank, then the solution to (3.3) is given by the Moore-Penrose pseudo-inverse

$$\boldsymbol{c} = \boldsymbol{V}^{+}\boldsymbol{b}. \tag{3.5}$$

The function $u(\boldsymbol{x})$ can then be approximated by a degree p polynomial given as $u_h(\boldsymbol{x}) = \boldsymbol{c}^T\boldsymbol{\mathcal{M}}(\delta\boldsymbol{x})$. Furthermore, any order ℓ linear differential operator can be approximated by applying the differential operator to the invididual monomial basis functions [19]

$$\mathcal{L}u(\boldsymbol{x}+\delta\boldsymbol{x}) \approx \boldsymbol{c}^T\mathcal{L}\boldsymbol{\mathcal{M}}(\delta\boldsymbol{x}) + \mathcal{O}\left(\|\delta\boldsymbol{x}\|_\infty^{d-l+1}\right). \tag{3.6}$$

One can also substitute (3.5) into (3.1) to get the an expression for a set of polynomials

$$u_h(\boldsymbol{x}+\delta\boldsymbol{x}) = \boldsymbol{b}^T\boldsymbol{V}^{+T}\boldsymbol{\mathcal{M}}(\delta\boldsymbol{x}) = \boldsymbol{b}^T\boldsymbol{\Phi}(\boldsymbol{x}+\delta\boldsymbol{x}) \tag{3.7}$$

where $\boldsymbol{\Phi}(\boldsymbol{x}+\delta\boldsymbol{x}) = \boldsymbol{V}^{+T}\boldsymbol{\mathcal{M}}(\delta\boldsymbol{x})$ is a group of polynomials associated with each vertex in the stencil.

Definition 1 (Generalized Lagrange Polynomials)**.** The *generalized Lagrange polynomials* of a stencil $\boldsymbol{X}$ are given by

$$\boldsymbol{\Phi} = \boldsymbol{V}^{+T}\boldsymbol{\mathcal{M}}(\delta\boldsymbol{x}). \tag{3.8}$$

The generalized Lagrange polynomials allow for the simple approximation of function values and their partial derivatives from the monomial basis in space. In general, $\boldsymbol{V}$ may be rank-deficient, either analytically or numerically, which will lead to a loss of accuracy under floating point arithmetic. Therefore, it is wiser to safeguard the computation of GLPBFs using a more stable version of $\boldsymbol{V}^{+}$. This is achieved by altering the least squares error of (3.4) with a *weighted least squares* error .

Let $w(d) = w(\|\boldsymbol{x}-\boldsymbol{x}_0\|)$ be a weighting function which satisfies $\lim_{d\to\infty} w(d) = 0$. The weighting function w will prioritize the minimization of errors for vertices, which are near the center of the stencil, $\boldsymbol{x}_0$. Throughout this dissertation, we work with weights of the form

$$w(d) = \frac{1}{(d/h+\epsilon)^{\alpha}},$$

where $\epsilon \ll 1$ is used to avoid a singularity at $d = 0$ and $\alpha > 0$ is an appropriate exponent which determines the rate of decay of the weighting

function. In this dissertation, we tend to use $\epsilon \approx 0.1$ and α to be one half of the degree of polynomial basis used in the weighted least squares approximation. Let $\boldsymbol{W} = \operatorname{diag}(w_0, w_1, \ldots, w_m)$, then the weighted least-squares solution becomes

$$\boldsymbol{c} = \arg\min_{\boldsymbol{x} \in \mathbb{R}^n} \|\boldsymbol{W}(\boldsymbol{V}\boldsymbol{x} - \boldsymbol{b})\|_2^2 .$$

Furthermore, the radius of the stencil could cause the columns of $\boldsymbol{V}$ or $\boldsymbol{W}\boldsymbol{V}$ to have different scales, which can be a source of ill-conditioning, which can affect the computation of (3.5). Therefore, the positions of the vertices are normalized to lie in the unit cube $[-1, 1]^d$ by right-multiplying the weighted Vandermonde matrix by the matrix

$$\boldsymbol{M} = \operatorname{diag}(\boldsymbol{\mathcal{M}}(\boldsymbol{h}))^{-1} .$$

The resulting weighted Vandermonde matrix is

$$\boldsymbol{A} = \boldsymbol{W}\boldsymbol{V}\boldsymbol{M}.$$

The matrix $\boldsymbol{A}$ has the property that every entry is $O(1)$ in magnitude, and usually has an improved condition number in comparison to the unscaled Vandermonde matrix $\boldsymbol{V}$. Equation (3.3) may then be rewritten as

$$\boldsymbol{A}\boldsymbol{z} \approx \boldsymbol{W}\boldsymbol{b},$$

and the weighted-least squares solution is now given by

$$\boldsymbol{c} = \boldsymbol{M}\boldsymbol{A}^{+}\boldsymbol{W}\boldsymbol{b}. \tag{3.9}$$

For full column rank Vandermonde systems, the solutions given by (3.5) and (3.9) will be equivalent under exact arithmetic [19]. Substituting (3.9) into (3.8) gives an equivalent expression for the GLPBFs

$$\boldsymbol{\Phi}\left(\boldsymbol{x}\right) = \boldsymbol{W}\boldsymbol{A}^{+T}\boldsymbol{M}\boldsymbol{\mathcal{M}}\left(\delta\boldsymbol{x}\right). \tag{3.10}$$

3.2 Numerical Stability of Computation

Generalized Lagrange polynomial basis functions allow for the estimates of partial derivatives and function values to be used inside the weak formulation. The matrix $\boldsymbol{A}$ is constructed so that the condition number $\kappa\left(\boldsymbol{A}\right) = O(1)$ if $\boldsymbol{V}$ is of full column rank. However in practice, the condition number of $\boldsymbol{A}$ may still be very large due to position of the points in the stencil. In this case, the GLPBFs must be constructed in a robust and numerically stable manner. The numerical rank of $\boldsymbol{A}$ is estimated by using a rank-revealing QR-factorization [12] with column pivoting (QRCP)

$$\boldsymbol{A}\boldsymbol{\Pi} = \boldsymbol{Q}\boldsymbol{R}. \tag{3.11}$$

The rank of $\boldsymbol{A}$ is then estimated from the numerical rank of $\boldsymbol{R}$ which can easily be computed by observing the diagonal entries. The matrix $\boldsymbol{A}$ is said to have numerical rank k if $|r_{k+1,k+1}| \leq \epsilon |r_{11}|$ with $\epsilon \ll 1$. If $\boldsymbol{A}$ is found to have numerical rank k, then only the first k columns of $\boldsymbol{A\Pi}$ are chosen, and the GLPBFs are computed as

$$\boldsymbol{\Phi}(\boldsymbol{x}) = \boldsymbol{W}\hat{\boldsymbol{Q}}_{:,1:k}\hat{\boldsymbol{R}}^{-T}_{1:k,1:k}\hat{\boldsymbol{\Pi}}^{T}_{:,1:k}\boldsymbol{M}\boldsymbol{\mathcal{M}}(\delta\boldsymbol{x}). \tag{3.12}$$

The use of QRCP guarantees that the GLPBFs computed will be consistent so long as the condition number of $\boldsymbol{A}$ is not too large. If the condition number is too large, then the order of consistency must be reduced to favor stability of the method. However this order of consistency only occurs if the truncated columns correspond to high-order terms. This assumption may be violated if the distribution of the stencils is unbalanced, such as when the stencil is situated near a boundary. These one-sided stencils are well-known in the finite difference literature and are often having a larger truncation error as opposed to the fully-balanced finite difference schemes [67]. Additionally, balanced finite difference schemes may also benefit from error cancellation and lower truncation error constants than unbalanced schemes.

To improve consistency of the scheme while still maintaining stability, an altered scheme must be used to ensure that columns of $\boldsymbol{A}$ corresponding to low-order terms are not thrown out before high order terms, which may depend on them. This is achieved by creating a direct acyclic graph (DAG)

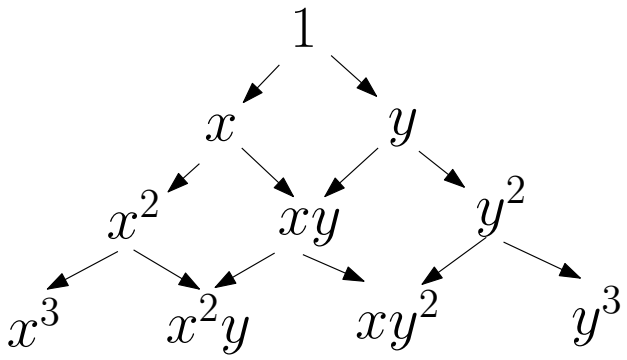

Figure 3.1: Pascal's triangle for bivariate monomials and the DAG representing priority relationships.

dependency graph based on Pascal's triangle or tetrahedron for bivariate or trivariate monomials as shown in Figure 3.1. The DAG is pruned as columns corresponding to the roots of the DAG are pivoted into position during the QRCP algorithm, and no high-order monomial may be chosen as a pivot unless all of its ancestors have already been removed from the DAG. The algorithm is terminated if the 2-norm of the columns corresponding to all available roots is less than a predefined tolerance ϵ. The description of the column pivoting strategy is shown in Algorithm 1.

3.3 Weak Formulation of AES-FEM

AES-FEM is traditionally constructed by computing a local stencil for each test function denoted by v_i, the ith test function of the traditional finite element family, as given by the mesh. Let $\phi_j(\boldsymbol{x})$ be the associated GLPBF of the jth vertex in the stencil $(\boldsymbol{X}_i, \boldsymbol{w}_i)$. Then the solution is approximated

Algorithm 1: Column Pivoting Strategy for QRCP.

input : A list of root monomials, list of parents remaining, and the parent-child dependency list for each monomial; Vandermonde matrix $\boldsymbol{A}$; tolerance ϵ

output: The QR-factorization of $\boldsymbol{A}$, a permutation vector $\boldsymbol{\pi}$, rank($\boldsymbol{A}$)

for *c = 1:ncols* **do**
  Find maximum column norm of all root monomials, store as k
  if $\|A_{c:end,k}\|_2 < \epsilon$ **then**
    `/* Truncate` $\boldsymbol{A}$ `and return permutation vector */`
    Set rank($\boldsymbol{A}$)=c-1
    return $\boldsymbol{A}_{:,1:r}$, $\boldsymbol{\pi}$
  end
  Swap $\boldsymbol{\pi}(c)$ and $\boldsymbol{\pi}(k)$, $\boldsymbol{A}_{:,c}$ and $\boldsymbol{A}_{:,k}$, and perform Householder reflection
  `/* Update DAG representation and add orphans to root list */`
  Remove root monomial from list of roots
  foreach *child of root* **do**
    Decrement parent count
    if *parent count == 0* **then**
      Add child to root list
    end
  end
end

by substituting

$$u_h = \sum_{j=1}^{n} u_j \phi_j$$

into the weak form

$$a\left(u_h, v_i\right) = F\left(v_i\right), \quad \forall i = 1, \ldots, n.$$

The resulting linear system of equations is

$$\boldsymbol{A}\boldsymbol{u} = \boldsymbol{b},$$

where

$$A_{ij} = a\left(\phi_j, v_i\right)$$
$$b_i = F\left(v_i\right).$$

The stiffness matrix $\boldsymbol{A}$ is in general nonsymmetric, but in practice is well-conditioned with proper choices of test functions.

In the assembly of the linear system, the stiffness matrix and load vector are constructed row by row for scalar problems such as Poisson or advection-diffusion, or block-row by block-row for problems of several variables (e.g. linear elasticity). The integration is performed in the same manner as traditional finite element matrices with mappings from a reference element to the individual mesh elements being computed. Let $\boldsymbol{J} = \frac{\partial \boldsymbol{x}}{\partial \boldsymbol{\xi}}$ be the Jacobian

of the isoparametric mapping from the reference element $\hat{K}$ to the physical element K. Then the integration over K is performed via the change of variables

$$\mathrm{d}K = \det \boldsymbol{J} \mathrm{d}\hat{K}.$$

The first-order partial derivatives of the test functions v are replaced with appropriate first order partial derivatives of the test functions $\hat{v}$ defined over $\hat{K}$,

$$\nabla_{\boldsymbol{x}} v = \boldsymbol{J}^{-T} \nabla_{\boldsymbol{\xi}} \hat{v}.$$

The partial derivatives of the GLPBFs are computed by determining the position of quadrature points in physical space using the parametric mapping provided by the mesh element. The numerical quadrature rules are exact for linear elements due to the fact that the GLPBFs are polynomials in physical and parametric space.

Neumann boundary conditions can be imposed in a similar manner to FEMs and computed using either prescribed data as in (2.4). In practice, the boundary data g may not be defined by an analytical function, but rather are only given by their values at the vertices and interpolated over the boundaries of the elements during load vector assembly. In the case of AES-FEM, the elements are linear, and the boundary data is only prescribed at the corner vertices of the elements. This could lead to an unacceptable loss of accuracy for high-order problems if only linear interpolation were used to estimate g at the boundary quadrature points. Therefore it becomes necessary to

approximate g *on the boundary* to high-order in addition to the high-order representation of the curved boundary itself. These issues are addressed in Chapters 4 and 5.

3.4 Results for High-Order AES-FEM

In this section, we assess the accuracy, efficiency, and element-quality dependence of AES-FEM with quadratic, quartic, and sextic basis functions, and compare it against FEM with linear, quadratic and cubic basis functions. The errors are calculated using the discrete L_2 and L_∞ norms. Let U denote the exact solution and let $\tilde{U}$ denote the numerical solution. Then, we calculate the norms as

$$L_2\,(\text{error}) = \left(\int_\Omega |\tilde{U} - U|^2 \partial\Omega\right)^{1/2} \quad \text{and} \quad L_\infty\,(\text{error}) = \max_i |\tilde{U} - U|. \tag{3.13}$$

On a series of meshes of different grid resolution, we calculate the average convergence rate as

$$\text{convergence rate } = -\log_2\left(\frac{\text{error on } m_c}{\text{error on } m_f}\right) \Bigg/ \log_2\left(\sqrt[d]{\frac{\text{nodes in } m_c}{\text{nodes in } m_f}}\right), \tag{3.14}$$

where d is the spacial dimension, m_c is the coarsest mesh, and m_f is the finest mesh.

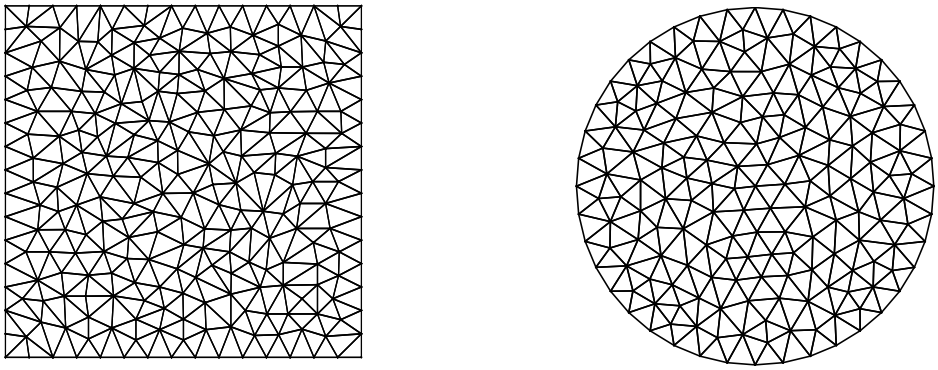

Figure 3.2: Example 2D meshes with linear elements.

3.4.1 2D Results

We first assess AES-FEM in 2D over the unit square and the unit disc, which are representative for geometries with flat and curved boundaries, respectively. We triangulated the domains using Triangle [61] for linear meshes and using Gmsh [29] for quadratic and cubic meshes. See Figure 3.2 for some examples meshes with linear elements, which are representative in terms of mesh quality but are coarser than those used in actual computations. The numbers of nodes for the unit square range from 1,027 to 146,077, and those for the unit disc range from 544 to 79,417. Since isoparametric FEM requires good mesh quality, we ensured that these meshes all have good element shapes for our comparative study: For linear meshes, the minimum angle is 24.04 degrees and the maximum angle is 128.17 degrees; for high-order meshes, all elements have positive Jacobians everywhere.

We consider the Poisson equation and convention-diffusion equation. For both cases, we use GMRES with the ILU preconditioner to solve the linear

systems arising from AES-FEM. For FEM, we use conjugate gradient (CG) with incomplete Cholesky as the preconditioner for the Poisson equation, and use GMRES with ILU for the convection-diffusion equation. To demonstrate the accuracy of high-order methods, we set the tolerance of the iterative solvers to 10^{-12}. The drop tolerance for the incomplete factorization is set as 10^{-4} by default, unless otherwise noted.

Poisson Equation

We first present results for the Poisson equation with Dirichlet boundary conditions on the unit square and on the unit disc. That is,

$$-\nabla^2 U = \rho \quad \text{in } \Omega, \tag{3.15}$$

$$U = g \quad \text{on } \partial\Omega. \tag{3.16}$$

For the unit square $\Omega = [0,1]^2$, we consider the following three analytic solutions:

$$U_1 = 16x^3(1-x^3)y^3(1-y^3), \tag{3.17}$$

$$U_2 = \cos(\pi x)\cos(\pi y), \tag{3.18}$$

$$U_3 = \frac{\sinh(\pi x)\cosh(\pi y)}{\sinh \pi \cosh \pi}. \tag{3.19}$$

For the unit disc $\Omega = \{(x, y)|x^2 + y^2 \leq 1\}$, we consider U_3 and also

$$U_4 = \cos\left(\frac{\pi}{2}\left(x^2 + y^2\right)\right).$$

For each problem, the right-hand side ρ and the Dirichlet boundary condition g are obtained from the given analytic solutions. For all the cases, the iterative solvers converged to the desired tolerance for AES-FEM. For FEM, the solver stagnated for the finest meshes in some cases without achieving the specified tolerance, even after we reduced the drop tolerance to 10^{-6} in incomplete Cholesky. However, the resulting errors were small enough not to affect the comparison qualitatively.

Figure 3.3 shows the L_∞ and L_2 norm errors for U_1 on the unit square. The L_2 norm errors for U_2 and U_3 on the unit square and for U_3 and U_4 on the unit disc are shown in Figures 3.4 and 3.5, respectively. In all cases, quadratic AES-FEM and linear FEM have similar errors, and quartic AES-FEM has similar or better results compared to cubic FEM. Both of the above pairs have similar sparsity patterns and similar numbers of nonzeros in the coefficient matrices. Furthermore, sextic AES-FEM is far more accurate than all the other methods, achieving sixth-order accuracy despite the use of linear elements. This result confirms our accuracy analysis in Section 3.3 for 2D problems.

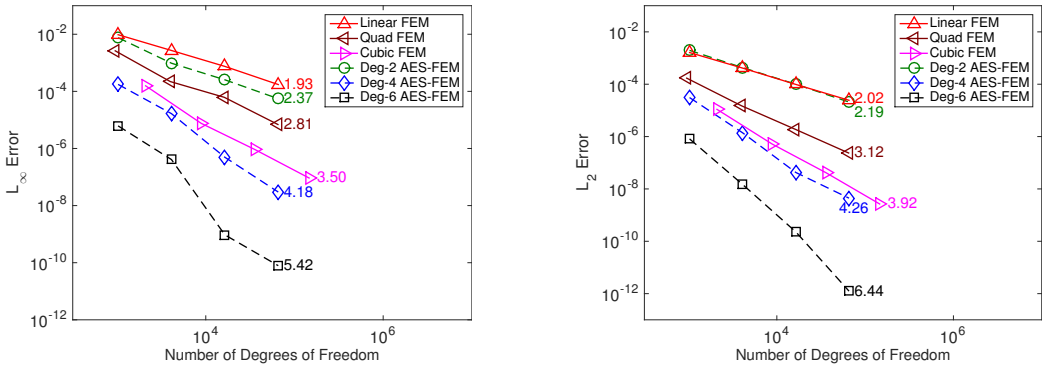

Figure 3.3: The errors for 2D Poisson equation on the unit square for U_1 in L_∞ (left) and L_2 norms (right). The number to the right of each curve indicates the average convergence rate.

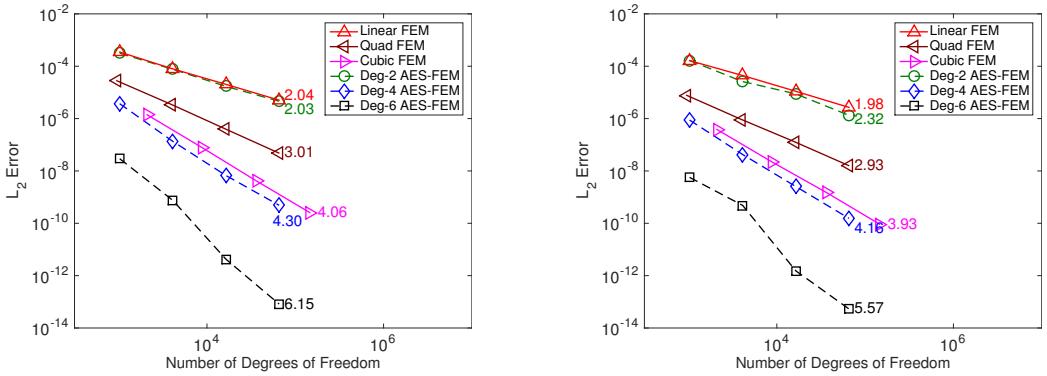

Figure 3.4: The L_2 norm errors for 2D Poisson equation on the unit square for U_2 (left) and U_3 (right).

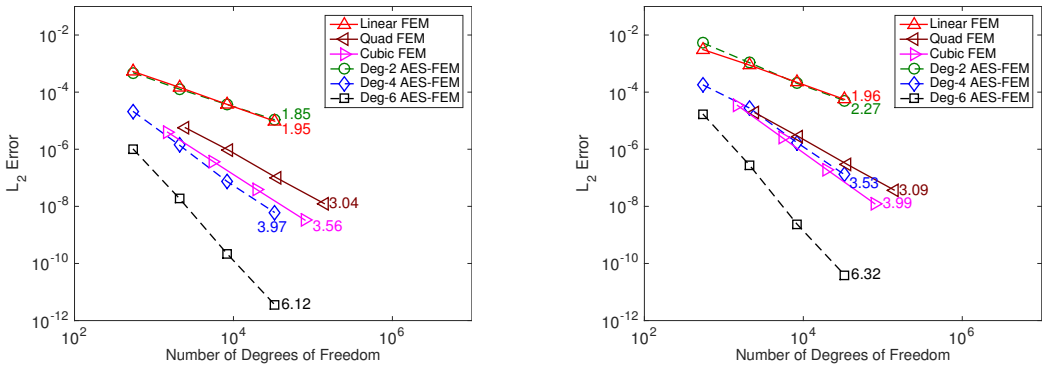

Figure 3.5: The L_2 norm errors for 2D Poisson equation on the unit disc for U_3 (left) and U_4 (right).

Convection-Diffusion Equation

In our second example, we consider the time-independent convection-diffusion equation with Dirichlet boundary conditions, that is,

$$-\nabla^2 U + \boldsymbol{c} \cdot \boldsymbol{\nabla} U = \rho \quad \text{in } \Omega, \tag{3.20}$$

$$U = g \quad \text{on } \partial\Omega. \tag{3.21}$$

We take $\boldsymbol{c} = [1, 1]^T$ for all of our tests, and we consider the same analytic solutions over the unit square and on the unit disc as for the Poisson equation.

Figure 3.6 shows the L_∞ and L_2 norm errors for U_1 on the unit square. The L_2 norm errors for U_2 and U_3 on the unit square and for U_3 and U_4 on the unit disc are shown in Figures 3.7 and 3.8, respectively. Similar to the Poisson equation, quadratic AES-FEM has similar convergence rate as linear FEM, but slightly lower errors. Quartic AES-FEM is more accurate than cubic FEM in all cases, and sextic AES-FEM again delivers superior

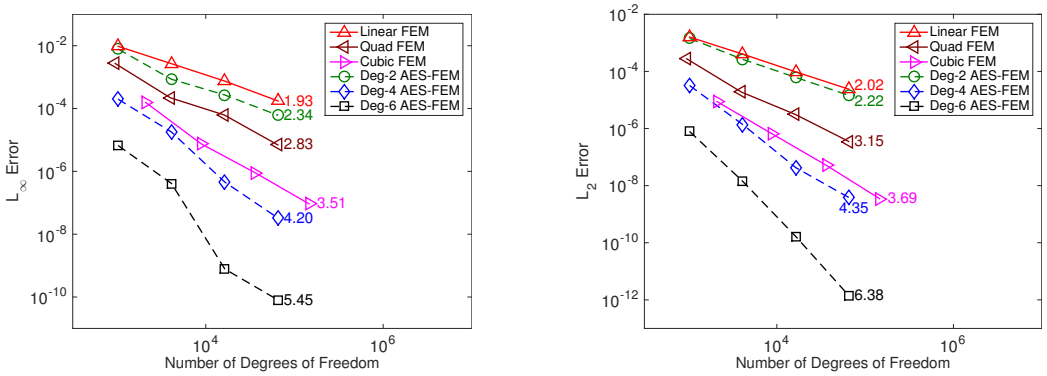

Figure 3.6: The errors for 2D convection-diffusion equation on the unit square for U_1 in the infinity norm (left) and the L_2 norm (right).

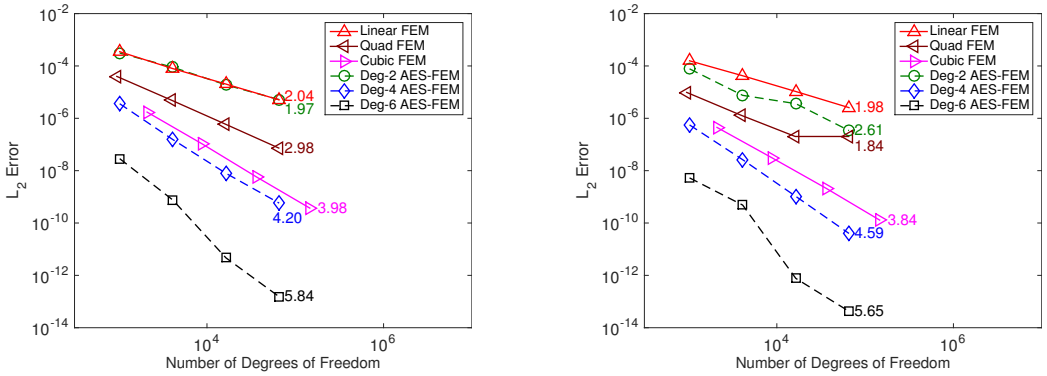

Figure 3.7: The L_2 norm errors for 2D convection-diffusion equation on the unit square for U_2 (left) and U_3 (right).

accuracy, achieving about sixth-order convergence.

3.4.2 3D Results

We now assess AES-FEM in 3D over the unit cube and the unit ball, which are representative for geometries with flat and curved boundaries, respectively. We mesh the domains using TetGen [65] for the linear meshes and

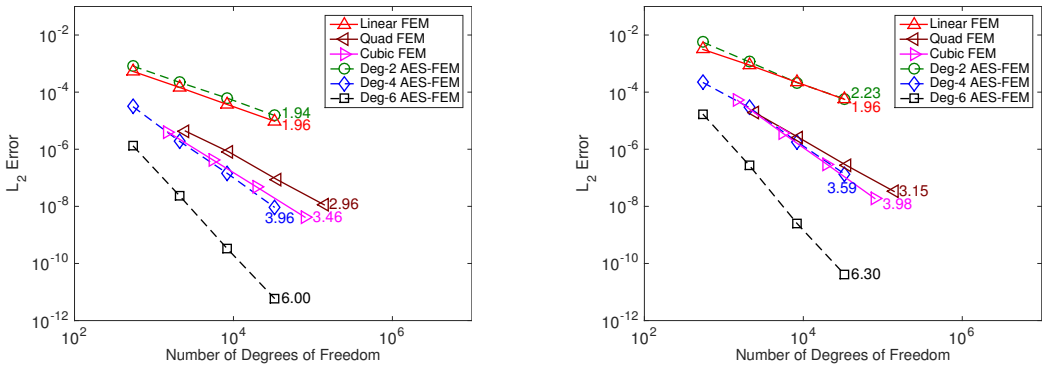

Figure 3.8: The L_2 norm errors for 2D convection-diffusion equation on the unit disc for U_3 (left) and U_4 (right).

using Gmsh for the quadratic and cubic meshes. See Figure 3.9 for some example meshes with linear elements, which are representative in terms of mesh quality but are coarser than those used in actual computations. The numbers of nodes for the unit cube range from 509 to 7,272,811, and those for the unit ball range from 1,011 to 2,834,229. As in 2D, since isoparametric FEM requires good mesh quality, we ensured that these meshes all have reasonable element shapes: For linear meshes, the minimum dihedral angle is 6.09 degrees and the maximum angle is 166.05 degrees; for high-order meshes, all elements have positive Jacobians everywhere.

We consider the Poisson equation and the convection-diffusion equation. For both cases, we use GMRES with the Gauss-Seidel preconditioner to solve the linear systems arising from AES-FEM. For FEM, we use CG with incomplete Cholesky as the preconditioner for the Poisson equation, and use GMRES with Gauss-Seidel for the convection-diffusion equation. We set the tolerance of the iterative solvers to 10^{-12}. The drop tolerance for incomplete

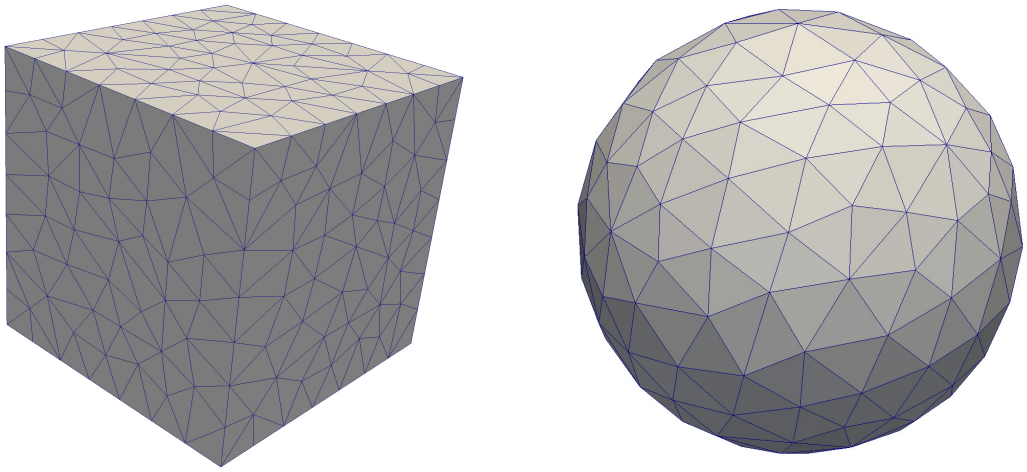

Figure 3.9: Example 3D meshes with linear elements.

Cholesky is 10^{-3} on the cube and 10^{-6} on the ball.

Poisson Equation

We first present results for the Poisson equation with Dirichlet boundary conditions on the unit cube and on the unit ball. That is,

$$-\nabla^2 U = \rho \quad \text{in } \Omega, \tag{3.22}$$

$$U = g \quad \text{on } \partial\Omega. \tag{3.23}$$

For the unit cube, where $\Omega = [0,1]^3$, we consider the following three analytic solutions:

$$U_1 = 64x^3\left(1-x^3\right)y^3\left(1-y^3\right)z^3\left(1-z^3\right), \tag{3.24}$$

$$U_2 = \cos(\pi x)\cos(\pi y)\cos(\pi z), \tag{3.25}$$

$$U_3 = \frac{\sinh(\pi x)\cosh(\pi y)\cosh(\pi z)}{\sinh\pi\cosh^2\pi}. \tag{3.26}$$

For the unit ball $\Omega = \{(x,y,z)|x^2+y^2+z^2 \leq 1\}$, we consider the analytic solution U_3 and also

$$U_4 = \cos\left(\frac{\pi}{2}\left(x^2+y^2+z^2\right)\right).$$

For each problem, the right-hand side ρ and the Dirichlet boundary conditions g are obtained from the given analytic solutions.

Figure 3.10 shows the L_∞ and L_2 norm errors for U_1 on the unit cube. The L_2 norm errors for U_2 and U_3 on the unit cube and for U_3 and U_4 on the unit ball are in Figures 3.11 and 3.12, respectively. In all cases, quadratic AES-FEM converges at similar or better rates than linear FEM and has lower errors, and quartic AES-FEM has similar or lower errors than cubic FEM. As in 2D, both of the aforementioned pairs have similar sparsity patterns and similar numbers of nonzeros in the coefficient matrices. Furthermore, sextic AES-FEM is far more accurate than all the other meshes, achieving sixth-order accuracy despite the use of linear elements. This further confirms

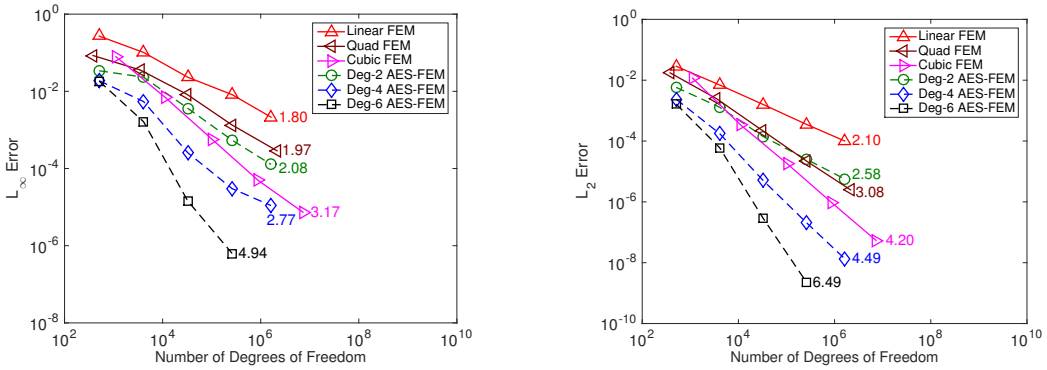

Figure 3.10: The errors for 3D Poisson equation on the unit cube for U_1 in the infinity norm (left) and L_2 norm (right).

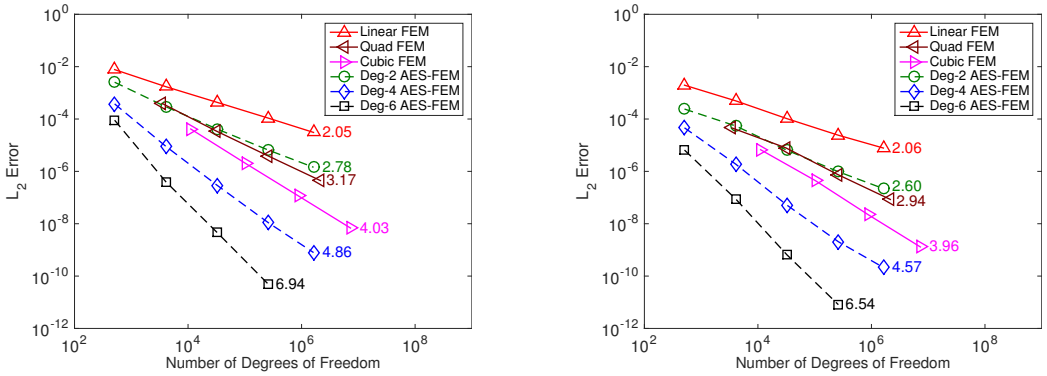

Figure 3.11: The L_2 norm errors for 3D Poisson equation on the unit cube for U_2 (left) and U_3 (right).

our accuracy analysis in Section 3.3 for 3D problems.

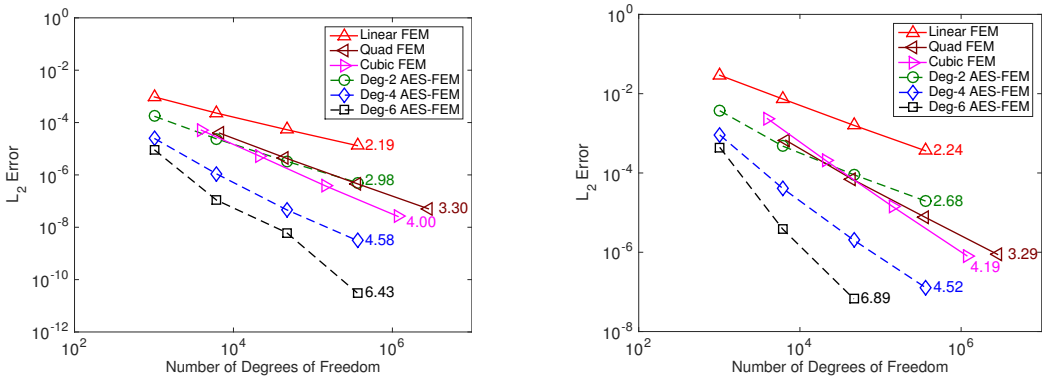

Figure 3.12: The L_2 norm errors for 3D Poisson equation on the unit ball for U_3 (left) and U_4 (right).

Convection-Diffusion Equation

We consider the time-independent convection-diffusion equation with Dirichlet boundary conditions on the unit cube and the unit ball, that is,

$$-\nabla^2 U + \boldsymbol{c} \cdot \boldsymbol{\nabla} U = \rho \quad \text{in } \Omega, \tag{3.27}$$

$$U = g \quad \text{on } \partial\Omega. \tag{3.28}$$

We take $\boldsymbol{c} = [1, 1, 1]^T$ and we consider the same analytic solutions over the unit cube and unit ball as for the Poisson equation.

Figure 3.13 shows the L_∞ and L_2 norm errors for U_1 on the unit cube. The L_2 norm errors for U_2 and U_3 on the unit cube and for U_3 and U_4 on the unit ball are in Figures 3.14 and 3.15, respectively. Similar to the Poisson equation, quadratic AES-FEM and linear FEM converge at similar rates with quadratic AES-FEM having slightly lower errors. Quartic AES-FEM is more

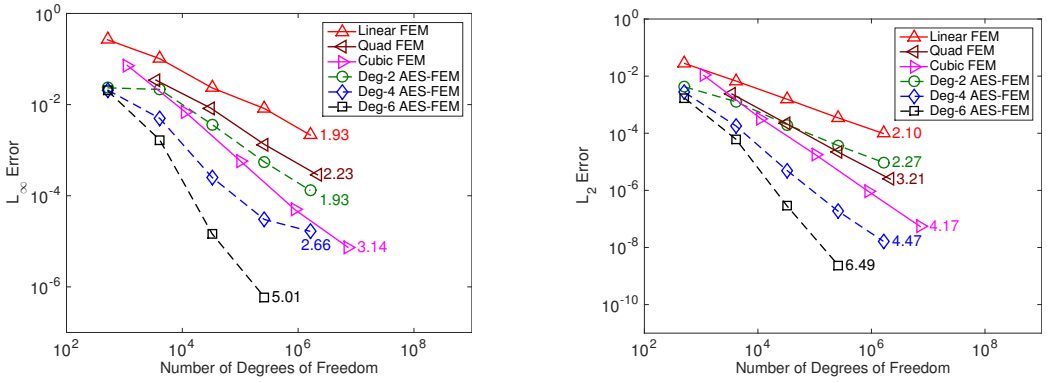

Figure 3.13: The errors for 3D convection-diffusion equation on the unit cube for U_1 in the infinity norm (left) and L_2 norm (right).

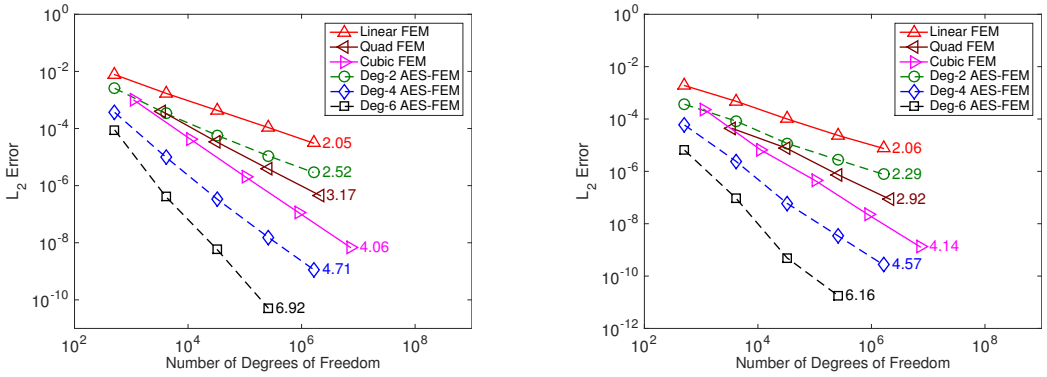

Figure 3.14: The L_2 norm errors for 3D convection-diffusion equation on the unit cube for U_2 (left) and U_3 (right).

accurate than the cubic FEM in all cases, and sextic AES-FEM is again the most accurate, with about sixth-order convergence. For FEM, the linear solver stagnated for the same problems on the finest mesh, but the resulting errors were small enough not to affect the comparison qualitatively.

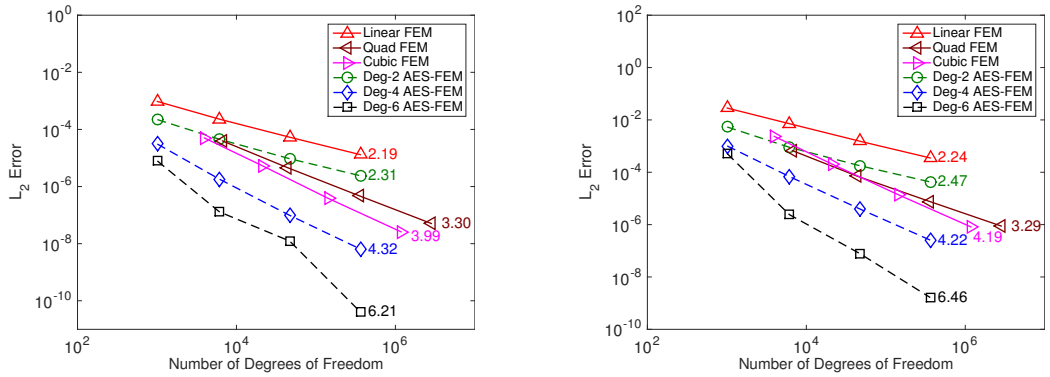

Figure 3.15: The L_2 norm errors for 3D convection-diffusion equation on the unit ball for U_3 (left) and U_4 (right).

Chapter 4

Treatment of Curved Geometries in AES-FEM

Geometry plays a critical role in the discretization of partial differential equations and their boundary conditions. This was well documented in [3] where the convergence of solving the 2D Euler Equations in discontinuous Galerkin finite element method (DGFEM) was shown to be highly dependent on the representation of the curved boundary. For AES-FEM, the goal is to maintain a high-order accurate solution on simplicial meshes without resorting to generating isoparametric meshes, which could be very large. An ideal situation would be to modify the simplicial meshes to conform to the curved boundary only for elements that are adjacent to the boundary. The first such method was proposed in [76], where the author constructed curved triangular elements that conformed exactly to the curved boundary. However, the map-

ping proposed is impossible to extend to three dimensions, which has led to the use of simpler high-order mappings based on quadratic approximations of the curved boundary [23]. Methods such as IGA [20]and NEFEM [59] have found success by using the exact NURBS geometry for problems when it is available. In particular, NEFEM only uses the exact NURBS geometry for elements adjacent to the boundary. This is attractive because the framework of classical Galerkin or DGFEM is conserved in the interior while special treatment is only required for a relatively small subset of elements near the boundary.

For AES-FEM, the order of accuracy is constrained by the accuracy of the representation of the geometry. Because partial derivatives are estimated via weighted least squares to high order, their consistency is guaranteed by construction. However for the integration of the weak form, geometry begins to play a role. This problem is especially critical for Neumann boundary conditions on the curved boundary, as the linear approximation of the boundary only allows for up to second order accuracy in practice.

In this chapter, we describe how the construction of high-order superparametric elements when given a parameterization of the geometry whether it be exact or an approximation. These superparametric elements allow for the accurate representation of the geometry in the discretization of the weak form. The procedure for generating the superparametric elements, similar to those presented in NEFEM [59, 60], but are used only for their geometric properties. Second, we discuss the needs for reconstructing the curved

boundary when no analytic representation, such as a parameterization or CAD model, is available We reconstruct the surface using weighted average of least squares fittings (WALF) [36] and use it to construct the curved elements.

4.1 Generation of High-Order Elements

At its heart, the GLPBFs share many similarities with meshless methods such as DEM [49] and EFG [7], because the GLPBFs are constructed from local weighted stencils for each test function without regard for "elements" defined by a mesh.[1] Therefore, the geometry must be described in order for numerical integration over the domain to be performed. Meshless methods generally tend to use simple quadrature rules for Cartesian grids with only a representation of the boundary overlayed on top of the integration domain. However, because one generally has a mesh in AES-FEM, the geometry and the domains of integration are determined by the elements of the mesh. The mesh itself necessary for AES-FEM to be consistent for several reasons. First, the mesh elements allow for the definition of compact weakly differentiable test functions, which are required for the weak form to be consistent. Second, the mesh elements allow for AES-FEM to use the same quadrature rules as traditional Galerkin elements

[1] By convention, AES-FEM selects the stencil by looking at *rings* of neighbors surrounding a vertex. This is effectively a geodesic metric rather than a Euclidean metric. However if the mesh is folded, other strategies such as k-nearest neighbor search can also be used.

The curved boundary itself may be given exactly (e.g. a CAD model, level set, or analytic function), but the exact representation of the geometry is not required. This idea was explored using NURBS surfaces in [59] for two dimensional DG problems and extended to three dimensional problems in [60]. In particular, in [60] the authors define several simple mappings which allow for the definition of curved tetrahedral elements along the boundary. These mappings are used for defining new reference elements for domains of integration.

The test functions in [60] may be polynomials defined on the reference element or polynomials defined in terms of the physical coordinates. The latter formulation is attractive because the partial derivatives of the basis functions is then guaranteed to be a polynomial, and the numerical quadrature rules may be exact [60]. However, continuity across curved element faces and edges is lost. This is acceptable for DG discretizations because the interelement discontinuities are accounted in the numerical fluxes across element faces. However, for the purposes of this dissertation, test functions must be continuous across element faces to ensure the consistency of AES-FEM without the need of integrating fluxes across element boundaries. Therefore, we construct *superparametric* elements, whose geometric shape functions are of higher degree polynomials than the degree of the test functions themselves [10, 14]. The superparametric elements will be both C^0-continuous as well as weakly differentiable, both of which are necessary for the weak formulation of second-order elliptic problems to be consistent. The superparametric test

functions are essential for representing the geometry of the boundary as well as formulating the weak formulation of the PDE in question. Therefore, to formulate the superparametric test functions, we need a local parameterization of the surface as well as C^0-continuity across element faces and edges.

4.1.1 Generation of Curvilinear Triangles

Let $\boldsymbol{C} : [0,1] \to \Gamma$ be a parameterization of a portion of the boundary with near the edge $\boldsymbol{x}_1\boldsymbol{x}_2$ of a triangle $K = \{\boldsymbol{x}_1, \boldsymbol{x}_2, \boldsymbol{x}_3\}$ arranged in counterclockwise orientation. Furthermore, suppose that $\boldsymbol{C}$ satisfies $\boldsymbol{C}(0) = \boldsymbol{x}_1$ and $\boldsymbol{C}(1) = \boldsymbol{x}_2$. In NEFEM, the curved element $\tilde{K}$ can be represented as the function

$$\boldsymbol{\Phi}(\xi, \eta) = (1 - \eta)\,\boldsymbol{C}(\xi) + \eta \boldsymbol{x}_3. \tag{4.1}$$

This effectively is a degenerate mapping of a unit square $[0,1]^2 \to K$, which enforces the curved boundary exactly. The parameterization of the boundary $\boldsymbol{C}$ could be either a spline/NURBS or derived from an analytical expression of the boundary.

The mapping provides a simple way to express geometry near a given surface, but for traditional FEM discretizations (or more generally *weighted residual* methods) at least C^0-continuity is required for integration by parts to be consistent.[2] The question becomes how to make parametric repre-

[2] A generalization to *nonconforming elements* is also possible but requires that interelement discontinuities be accounted for in the weak formulation. Examples of these

sentations of these mappings that are nonsingular but that also preserve continuity across element edges with both adjacent curvilinear elements and linear simplex elements.

Definition 2. Given a linear simplex element $K = \{\boldsymbol{x}_1, \boldsymbol{x}_2, \boldsymbol{x}_3\}$, with $\boldsymbol{x}_1\bar{\boldsymbol{x}}_2$ lying adjacent to the boundary, and let $\boldsymbol{C}$ be a parameterization which satisfies condition above. Then for any parametric coordinate (ξ, η) the point $\boldsymbol{x}(\xi, \eta) \in \tilde{K}$ given by

$$\boldsymbol{x}(\xi, \eta) = (1 - \eta)\, \boldsymbol{C}\left(\bar{\xi}\right) + \eta \boldsymbol{x}_3,$$

with

$$\bar{\xi} = \begin{cases} \frac{\xi}{1-\eta}, & \text{if } \eta > 0, \\ 0, & \text{if } \eta = 0. \end{cases}$$

Using this parameterization, we can place points from the traditional Lagrange points in parametric space with vertices in physical space as shown in Figure 4.1. The Lagrange points are placed on equally spaced points on the parametric *reference* element. Since the new Lagrange points only represent the geometry, the test functions are chosen to vary linearly on the *reference element*. Due to the placement of the Lagrange points, C^0-continuity follows.

Once the parameterization of the surface has been defined (either through exact geometry, CAD model, or WALF-reconstruction), then the shape functions of the element must be constructed. In particular, Lagrange vertices

nonconforming elements include Raviart-Crouzeix [22] and Raviart-Thomas [53] elements.

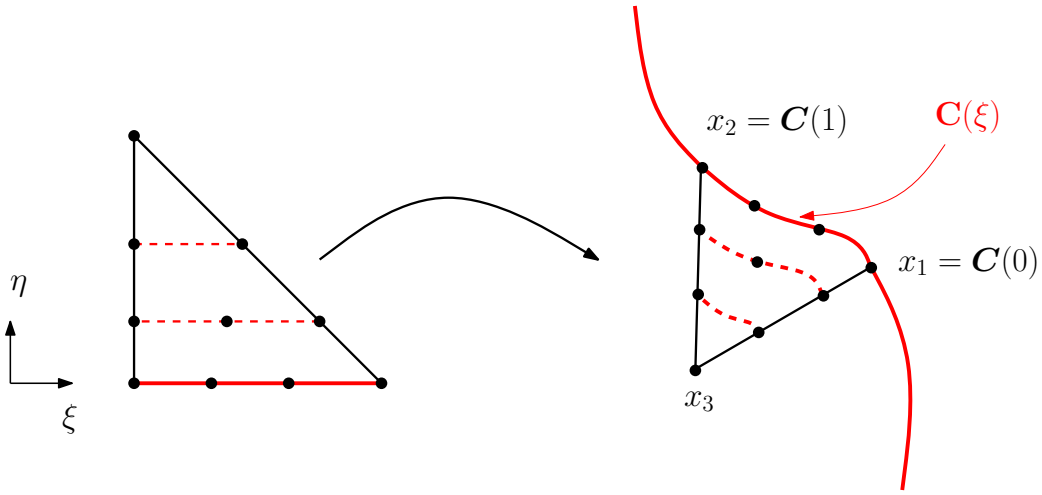

Figure 4.1: Parameterization used to generate superparametric elements from parameterized portion of boundary.

must be strategically placed in the element to guarantee C^0 continuity along the element faces and edges while maintaining a nonsingular Jacobian of the parametric transformation throughout the interior of the element. In particular, curved elements may be adjacent to linear simplex elements that exist inside of the interior. High-order Lagrange nodes on the straight-edged faces/edges of these elements can be placed in traditional equidistant configurations or along Fekete point distributions. Then along these edges and faces, the superparametric geometry will align exactly with the geometry of the linear elements of the interior.

Lemma 3. *Let K be a curvilinear triangle with test functions v_1, v_2, v_3*

defined as the traditional linear test functions on the unit circle

$$v_1(\xi, \eta) = 1 - \xi - \eta$$
$$v_2(\xi, \eta) = \xi$$
$$v_3(\xi, \eta) = \eta.$$

Then the test functions are C^0-continuous across edges.

The distribution of interior superparametric nodes is more involved due to the stringent constraints that the parametric mapping must be diffeomorphic between the reference element and the physical element. Therefore, it becomes desirable to choose interior vertex positions that lead to nonsingular Jacobians *a priori*. This is further complicated by the fact that curved elements in three dimensions occur when the element has either one face or one edge along the curved boundary, while curved elements in two dimensional meshes only occur if a single edge is located on the curved boundary. Fortunately, several mappings are provided in [59, 60], which allow for the simple placement of points inside the superparametric elements.

In the two dimensional case, only elements with one edge on the curved boundary will need to be treated. Using the parametric representation of (4.1) allows for simple placement of the Lagrange points, which can satisfy both C^0 continuity and curved representation of the geometry.

Algorithm 2: Placement of high-order vertices for superparametric triangles.

input : A linear triangle $\boldsymbol{x}_1\boldsymbol{x}_2\boldsymbol{x}_3$, a parameterization $\boldsymbol{C}(\xi)$ over $\overline{\boldsymbol{x}_1\boldsymbol{x}_2}$
output: The location of Lagrange vertices of superparametric element

foreach *corner vertex in linear triangle* **do**
  Store in high-order triangle
end
foreach *edge opposite of interior triangle* **do**
  Compute equidistant vertices on edge and store in high-order triangle
end
Compute equidistant vertices on curve
foreach *interior vertex coordinate* (ξ, η) **do**
  Compute position $\boldsymbol{x}_{\text{hi}} = (1-\eta)\boldsymbol{C}(\bar{\xi}) + \eta\boldsymbol{x}_3$
end

4.1.2 Generation of Curvilinear Tetrahedra

In three dimensions, there are more conditions that need to be satisfied to guarantee C^0 continuity because elements may be curved whenever they have one face or one edge on the curved boundary. Let (ξ, η, ζ) be the coordinates of the reference element. Then for curved tetrahedron, we assume that the curved face will lie on the $(\xi, \eta, 0)$ face, and that any curved edge will mapped from the $(\xi, 0, 0)$ edge.

For any element K with a face lying on the curved boundary Γ, let $\boldsymbol{C}(\xi, \eta)$ be a local parameterization of Γ over the face of the element with $\boldsymbol{C}(0,0) = \boldsymbol{x}_1$, $\boldsymbol{C}(1,0) = \boldsymbol{x}_2$, $\boldsymbol{C}(0,1) = \boldsymbol{x}_3$. Let $\tilde{K}$ be the reference tetrahedra for a high-order element. Then the Lagrange nodes for the vertices can be placed

at

$$\boldsymbol{x}\left(\xi,\eta,\zeta\right)=\left(1-\zeta\right)\boldsymbol{C}\left(\overline{\xi},\overline{\eta}\right)+\zeta\boldsymbol{x}_4, \tag{4.2}$$

where

$$\overline{\xi}=\begin{cases}\frac{\xi}{1-\zeta} & \text{if } \zeta>0,\\ 0 & \text{if } \zeta=0,\end{cases}$$

$$\overline{\eta}=\begin{cases}\frac{\eta}{1-\zeta} & \text{if } \zeta>0,\\ 0 & \text{if } \zeta=0.\end{cases}$$

The mapping (4.2) is shown in Figure 4.2.

For elements with only a single edge lying on the boundary, the mapping is a bit more involved. For an element K with corner vertices $\boldsymbol{x}_1$ and $\boldsymbol{x}_2$ lying on the curved boundary, let $\boldsymbol{C}\left(\xi\right)$ be a parameterization of curve. Then for any vertex with coordinates $(\xi,\eta,\zeta)\in\tilde{K}$, the vertex will be placed at the point

$$\begin{aligned}\boldsymbol{x}\left(\xi,\eta,\zeta\right)&=\left(1-\zeta\right)\boldsymbol{\Theta}\left(\overline{\xi},\overline{\eta}\right)+\zeta\boldsymbol{x}_4\\ \boldsymbol{\Theta}\left(\overline{\xi},\overline{\eta}\right)&=\left(1-\overline{\eta}\right)\boldsymbol{C}(\overline{\overline{\xi}})+\overline{\eta}\boldsymbol{x}_3\end{aligned} \tag{4.3}$$

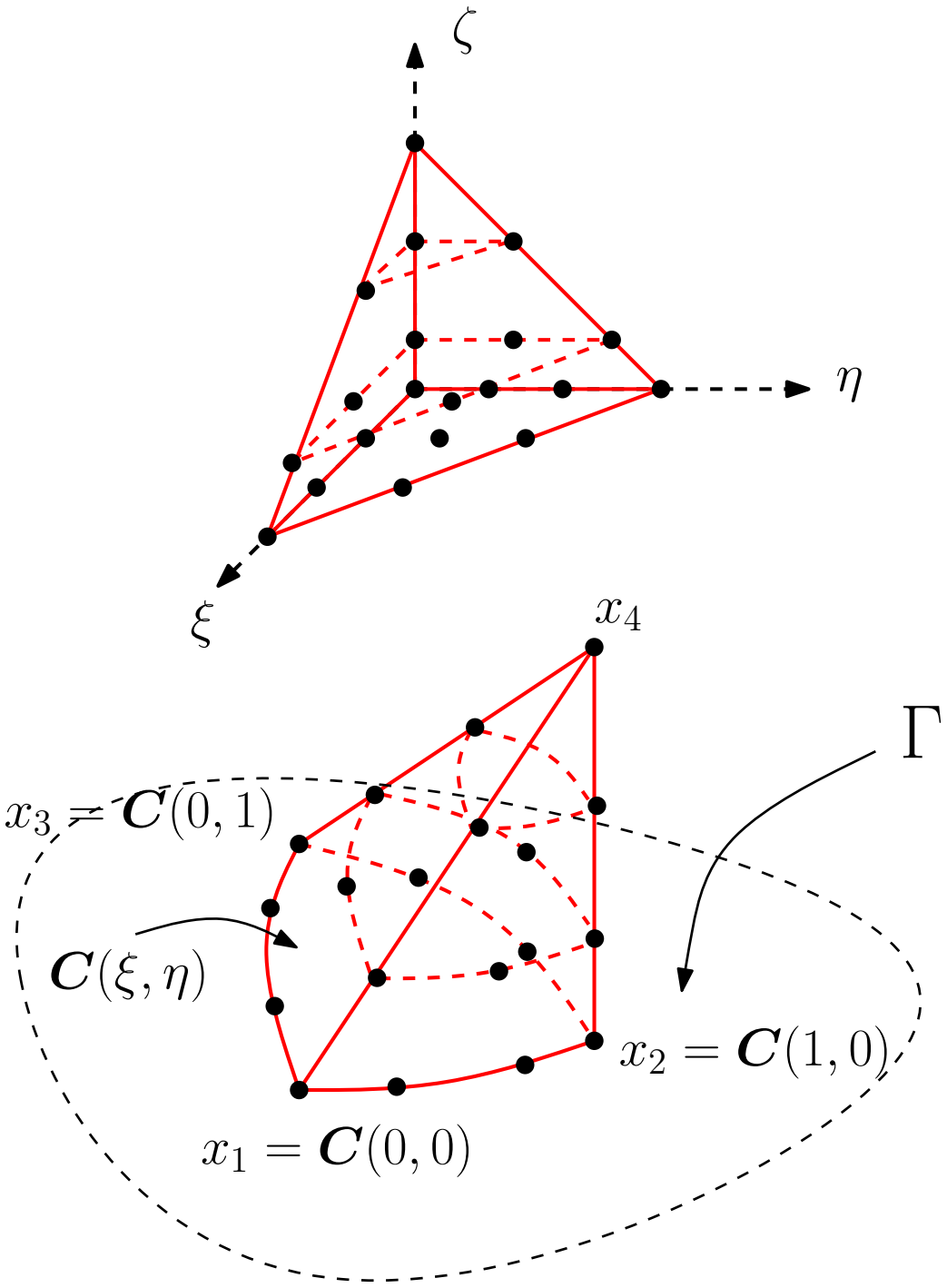

Figure 4.2: Curvilinear mapping for tetrahedron with a face on curved boundary.

where

$$\overline{\xi} = \begin{cases} \frac{\xi}{1-\zeta} & \text{if } \zeta > 0, \\ 0 & \text{if } \zeta = 0, \end{cases}$$

$$\overline{\eta} = \begin{cases} \frac{\eta}{1-\zeta} & \text{if } \zeta > 0, \\ 0 & \text{if } \zeta = 0. \end{cases}$$

$$\overline{\overline{\xi}} = \begin{cases} \frac{\overline{\xi}}{1-\overline{\eta}} & \text{if } \overline{\eta} > 0 \\ 0 & \text{if } \overline{\eta} = 0. \end{cases}$$

For this parameterization, the tetrahedron has two curved sides adjoining the curved edge while also having two planar faces that connect each vertex on the surface with the two interior vertices.

The parameterizations again have C^0-continuity of test functions when the test functions are chosen to linearly vary over the reference element.

4.2 Weighted Averaging of Local Fittings (WALF)

Geometries for many applications in biology, physics, and engineering are too prohibitive to model exactly either because the geometry is only given by a discrete set of points or is deforming too much to be able to use an exact representation such as NURBS or T-splines. This necessitates the high-order reconstruction of the geometry using only the information available at mesh vertices, and we accomplish this using WALF [36]. In WALF, local

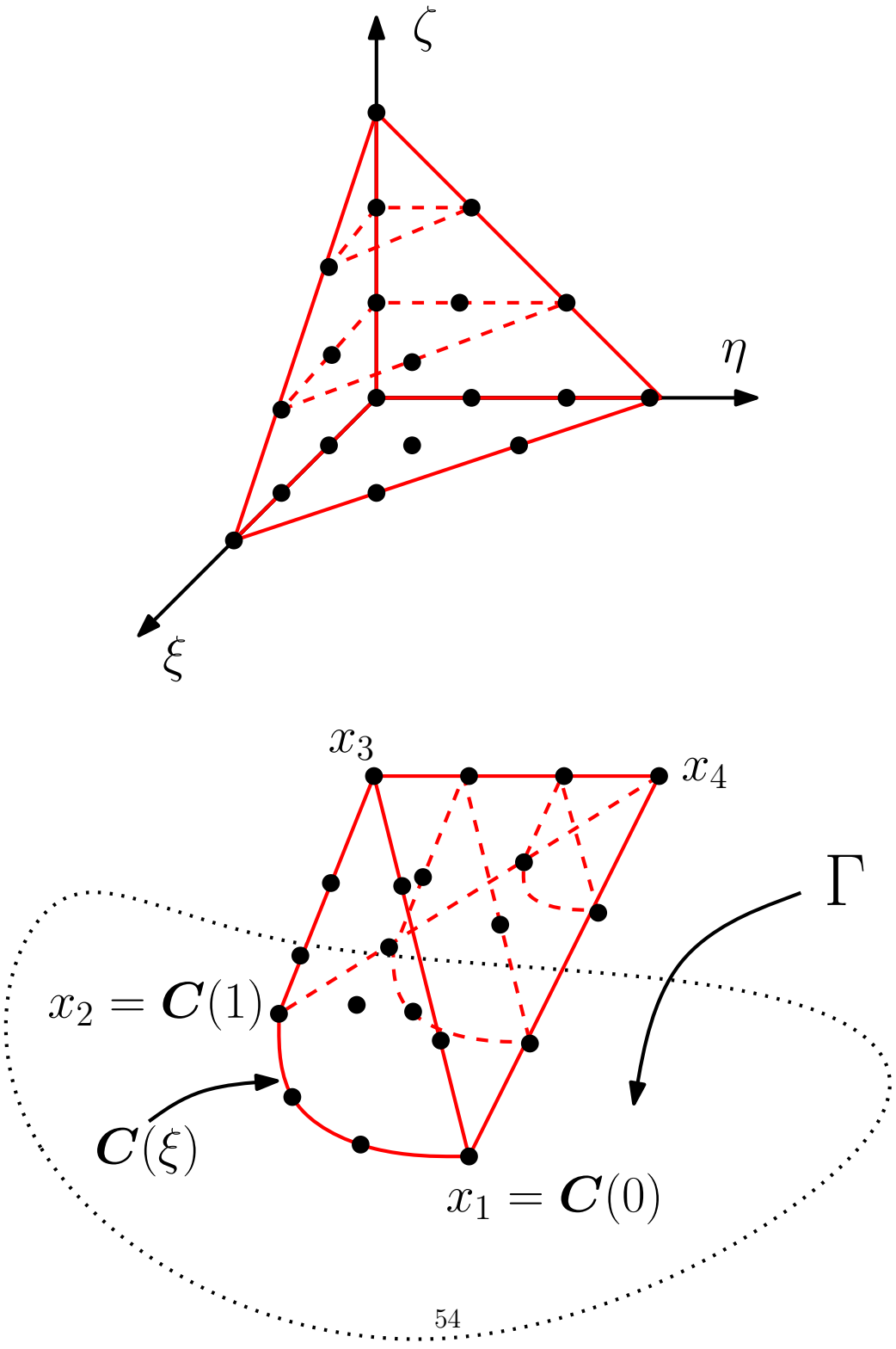

Figure 4.3: Construction of a curvilinear tetrahedron with one edge on the curved boundary.

polynomial fittings of the surface are blended together using piecewise linear finite shape functions. Additionally, it was shown in [54] how to use WALF reconstructions of discrete surfaces to perform high-order integration over surfaces using only discrete data given at the nodes.

The weighted average of least squares fittings (WALF) allows for the reconstruction of surfaces only given a discrete set of points on the surface [35, 36]. In practice, the parameterization $\boldsymbol{x}(\boldsymbol{u})$ may not be given exactly and must be reconstructed. This reconstruction is performed as a weighted average of least squares fittings (WALF), where local parameterizations of the surface Γ are chosen to be approximated by polynomial local height functions [36]. For each vertex $\boldsymbol{x}_i$ of a linear mesh, assume that $\hat{\boldsymbol{m}}_i$ is a unit normal vector which approximates the true unit normal to at least first order. At $\boldsymbol{x}_i$ we may construct a local coordinate system given by the column vectors of the matrix

$$\boldsymbol{Q}_i = \left[\hat{\boldsymbol{t}}_1 | \hat{\boldsymbol{t}}_2 | \hat{\boldsymbol{m}}_i\right], \tag{4.4}$$

where $\hat{\boldsymbol{t}}_j$, $j = 1, 2$, are unit vectors orthogonal to $\hat{\boldsymbol{m}}_i$ which approximate the tangent space of Γ.

Given a collection of n vertices $\boldsymbol{X}_i = \{\boldsymbol{x}_0, \boldsymbol{x}_1, ..., \boldsymbol{x}_{n-1}\}$ about a vertex x_i, with $\boldsymbol{x}_0 \equiv \boldsymbol{x}_i$ by convention, the vertices may be transformed into the local coordinate system (4.4), giving a set of point positions $\boldsymbol{U} = \{(u_j, v_j, f(u_j, v_j))\}_{j=0}^{n-1}$, where $f : U \to \mathbb{R}$ is the height function of the surface in the local coordinate

frame. We approximate f as a degree-d Taylor series

$$f(u,v) = \sum_{p=0}^{d} \sum_{r+s=p} c_{rs} u^r v^s + \sum_{r+s=d+1} \tilde{c}_{rs} u^r v^s, \tag{4.5}$$

where $c_{rs} = \frac{1}{r!s!} \frac{\partial^{r+s} f}{\partial u^r \partial v^s}(0,0)$ and $\tilde{c}_{rs} = \frac{1}{r!s!} \frac{\partial^{r+s} f}{\partial u^r \partial v^s}(\tilde{u},\tilde{v})$ for $0 \leq \tilde{u} \leq u$, $0 \leq \tilde{v} \leq v$. Equation (4.5) is solved approximately by solving a linear system

$$\boldsymbol{V}\boldsymbol{c} \approx \boldsymbol{f}, \tag{4.6}$$

where $\boldsymbol{V}$ is the Vandermonde matrix, $\boldsymbol{c}$ is a vector with unknowns c_{rs}, and $\boldsymbol{f}$ is a vector of the height function values of the surface. If $\boldsymbol{V}$ is of full column rank, then the least squares solution to (4.6) is unique and given by

$$\boldsymbol{c} = \boldsymbol{V}^{+}\boldsymbol{f}, \tag{4.7}$$

where $\boldsymbol{V}^{+}$ is the pseudo-inverse of $\boldsymbol{V}$.

Often, the condition number of (4.6) can be very large. This may lead to a loss of accuracy in the computation of (4.7). To ensure robustness of the linear system, row weighting and column scaling are applied to the local Vandermonde matrix to improve the condition number, resulting in the linear system

$$\boldsymbol{A}\boldsymbol{z} \approx \boldsymbol{W}\boldsymbol{f}. \tag{4.8}$$

If the rescaled Vandermonde system is still ill-conditioned, then (4.8) is solved

using truncated QR factorization with column pivoting to effectively reduce the high-order terms which contribute to the instability [36].

Let $\tilde{f}(u,v) = \sum_{p=0}^{d} \sum_{r+s=p} c_{rs} u^r v^s$ be the *local height function* of the local coordinate frame at some point (u,v), then the corresponding point in physical space is given by

$$\boldsymbol{p}_i(u,v) = \boldsymbol{Q} \begin{bmatrix} u \\ v \\ \tilde{f}(u,v) \end{bmatrix} + \boldsymbol{x}_i = u\hat{\boldsymbol{t}}_1 + v\hat{\boldsymbol{t}}_2 + \tilde{f}(u,v)\,\hat{\boldsymbol{m}}_i + \boldsymbol{x}_i. \tag{4.9}$$

Let $\{\boldsymbol{x}_1, \boldsymbol{x}_2, \boldsymbol{x}_3\}$ be vertices at the corner of a linear triangle K located approximately on the surface, and denote the finite element shape functions defined on K as $N_i(\xi,\eta)$. The WALF-reconstructed surface is then given as a weighted averaging of the local fittings

$$\boldsymbol{p}(\xi,\eta) = \sum_{i=1}^{3} N_i(\xi,\eta)\,\boldsymbol{p}_i(\xi,\eta). \tag{4.10}$$

The WALF-reconstructed surface (4.10) allows for a high order reconstruction of the ideal surface when given only a linear surface mesh and is necessary for high-order convergence.. For future use we give the following theorem whose proof can be found in [36]

Theorem 4. *Let $\boldsymbol{p}$ be a degree-d WALF-reconstructed surface in (4.10) of some smooth surface Γ. Then $\boldsymbol{p}$ approximates Γ to $\mathcal{O}\left(h^{d+1} + h^6\right)$.*

The bounds of Theorem 4 are somewhat pessimistic because of the mis-

matching local coordinate frames over each element. However for many applications, sixth order accuracy is more than sufficient.

4.3 Interpolation of Neumann Boundary Conditions

High-order representation of the Neumann boundary conditions must also be transferred from the linear mesh. If there is an analytic formula for the boundary conditions, then they can be transferred to the curved boundary exactly. It is often the case that only the values of the Neumann boundary conditions are given for the degrees of freedom located within the mesh. This requires that the data be interpolated on the boundary to high-order to maintain high-order accuracy. For AES-FEM, we are only given the associated boundary conditions at the vertices of a linear triangular or tetrahedral mesh; therefore the Neumann boundary conditions must be reconstructed at the quadrature points if an analytic expression for them is not given.

For each test function on the surface, the function g is locally reconstructed using the data from the neighbors on the surface. Suppose that $\Gamma_h = \bigcup_i K_i$ for a set of curvilinear elements K_i over which the test function v_i has support. Then the surface integral may be computed using quadrature rules defined over the surface lines or triangles as shown in [55]. The coefficients of the local polynomial approximations to g can be precomputed and evaluated at the quadrature points, or it can be computed on the fly.

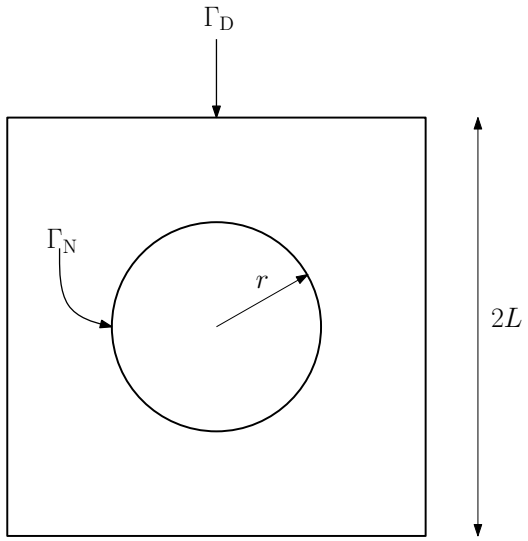

Figure 4.4: Domains for Poisson equation with curved and linear geometries.

4.4 Numerical Experiments

We present numerical experiments for various PDEs on some domains involving curved geometries. First, we will explore the effects of curved geometry on the convergence of AES-FEM for simple Poisson equation in two and three dimensions under both Dirichlet and Neumann boundary conditions using linear test functions. Second, we will then consider the superparametric elements described in Section 4.1

4.4.1 Two Dimensional Poisson Equation

We begin by providing a couple of numerical tests for Poisson equation using the two domains shown in Figure 4.4. In the numerical experiments, the values of $L = 1$ and $r = 0.5$ are chosen. Both geometries are relatively simple

Table 4.1: Convergence for two dimensional Poisson equation on curved hole with Dirichlet conditions on inner hole.

	#DOFs	152	540	1992	7716	Convergence Rate
GLPBF Deg.	Quadratic	2.84e-1	6.36e-2	1.00e-2	1.52e-3	2.66
	Cubic	1.13e-1	5.47e-2	1.56e-2	3.99e-3	1.70
	Quartic	7.96e-3	8.75e-4	6.11e-5	2.90e-6	4.0
	Quintic	5.16e-3	9.03e-4	7.07e-5	5.46e-6	3.49
	Sextic	2.302e-3	4.03e-5	1.29e-6	1.84e-8	5.98

but display the importance of the representing the geometry to high order even for simple problems with nontrivial boundary conditions. A sequence of linear simplex meshes were constructed using Gmsh [29], and both the linear mesh and the reconstructed geometries are considered.

The solution considered is

$$u_1(x_i) = \left(\prod_{i=1}^{d}\left(1 - x_i^2\right)\right)\left(1 - 4\sum_{i=1}^{d} x_i^2\right)^2. \tag{4.11}$$

The forcing function is computed analytically by applying the Laplace operator to (4.11).

The results for the two dimensional problem with the round hole show that a high order representation of the geometry is required in order to achieve high order convergence. As expected, the curved geometry with the round hole has numerous challenges for high order convergence due to the prevalence of geometric errors near the interior hole. Figure 4.5 shows that the convergence rate for the Poisson equation with Neumann boundary conditions are more or less the same regardless of the These geometric errors

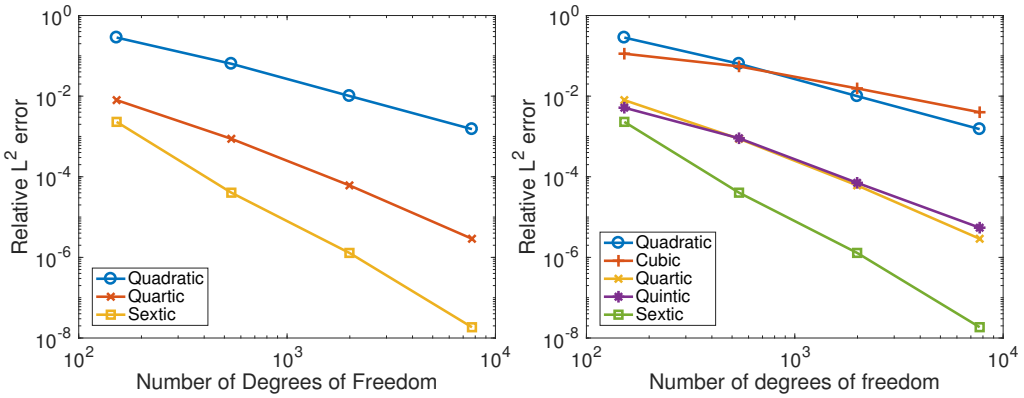

Figure 4.5: Results for two dimensional Poisson Equation with pure Dirichlet boundary conditions on curved domain using linear (left) and superparametric (right) test functions.

Table 4.2: Table of convergence for two dimensional Neumann problem using linear test functions.

	#DOFs	152	540	1992	7716	Convergence Rate
GLPBF Deg.	Quadratic	3.16e-1	6.68e-2	1.19e-2	1.60e-3	2.69
	Cubic	3.28e-1	1.46e-1	4.04e-2	1.01e-2	1.77
	Quartic	2.72e-2	2.67e-3	7.54e-4	2.08e-4	2.48
	Quintic	4.49e-3	4.82e-3	9.41e-4	2.18e-4	1.54
	Sextic	1.13e-2	3.48e-3	8.33e-4	2.10e-4	2.03

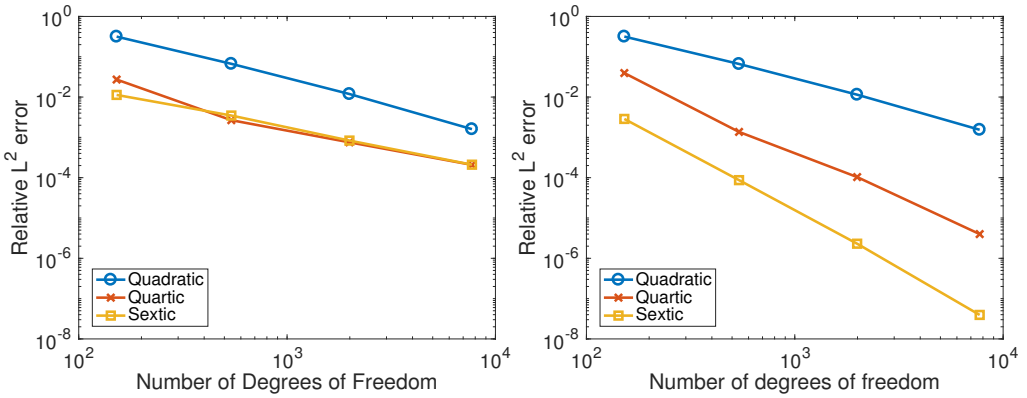

Figure 4.6: Convergence plot for AES-FEM for Poisson equation with Neumann boundary conditions on curved domain using linear (left) and superparametric test functions. .

	#DOFs	152	540	1992	7716	Convergence Rate
GLPBF Deg.	Quadratic	2.84e-1	6.36e-2	1.01e-2	1.52e-3	2.66
	Cubic	1.13e-1	5.47e-2	1.56e-2	3.99e-3	1.70
	Quartic	7.97e-3	8.75e-4	6.11e-5	2.90e-6	4.03
	Quintic	5.17e-3	9.02e-4	7.07e-5	5.46e-6	3.49
	Sextic	2.30e-3	4.03e-5	1.29e-6	1.85e-8	5.97

Table 4.3: Table of convergence for two dimensional Dirichlet problem.

become a limiting factor when Neumann boundary conditions are present as the test functions are nonzero near the boundary. However for Dirichlet boundary conditions, the test functions vanish near the boundary and hence the weighted residuals do not penalize the error near the boundary as much.

Figure 4.6 shows the convergence plot for the two domain using curved elements on the round hole with Tables 4.3 and 4.4 showing the numerical errors and rates of convergence for each choice of basis function.

The degree of the shape functions of the curved elements are chosen to

	#DOFs	152	540	1992	7716	Convergence Rate
GLPBF Deg.	Quadratic	3.17e-1	6.62e-2	1.15e-2	1.54e-3	2.71
	Cubic	3.18e-1	1.43e-1	3.96e-2	9.93e-3	1.77
	Quartic	3.94e-2	1.37e-3	1.04e-4	3.99e-6	4.69
	Quintic	1.32e-2	1.45e-3	1.21e-4	8.70e-6	3.73
	Sextic	2.87e-3	8.69e-5	2.30e-6	3.94e-8	5.50

Table 4.4: Table of convergence for two dimensional Neumann problem.

be equal to the degree of the

4.4.2 Three Dimensional Poisson Equation

The Poisson equation is again solved on a simple three dimension domain with a cube $\Omega = [-1,1]^3 \setminus B(0,0.5)$, and homogeneous boundary conditions $u|_{\Gamma_D} = 0$ on the exterior boundary. On the interior curved boundary, either pure Dirichlet conditions or pure Neumann boundary conditions are imposed. Superparametric elements are constructed by projecting the appropriate Lagrange points on the boundary faces and edges onto the spherical hole. The other Lagrange points are interpolated based on (4.2) and (4.3). The resulting linear systems are solved using Petsc's GMRES implementation with ILU preconditioning using SuperLU.

Figure 4.7 shows the convergence of AES-FEM with curved superparametric test functions for pure Dirichlet boundary. The orders of convergence are listed in Tables 4.5 and 4.6. Although quadratic basis functions do not have optimal convergence, high degree polynomial bases enjoy very good convergence rates. The benefits of using the high degree polynomials allows for

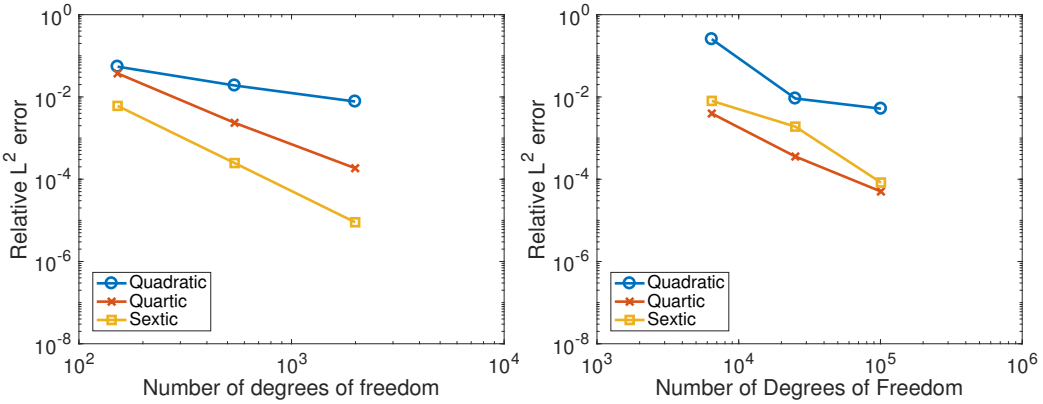

Figure 4.7: Convergence results for curved geometry with curved superparametric elements for Dirichlet (left) and Neumann (right) boundary conditions.

Table 4.5: Table of convergence for three dimensional Dirichlet Problem with curved test functions.

	#DOFs	6458	25,084	100,772	Convergence Rate
GLPBF Deg.	Quadratic	1.8264e-2	8.5774e-3	4.9821e-3	1.419
	Cubic	6.5279e-2	2.6985e-2	1.0527e-2	1.992
	Quartic	2.6384e-3	3.5349e-4	4.2339e-5	4.512
	Quintic	1.3208e-3	2.0118e-4	2.5777e-5	4.298
	Sextic	5.5690e-4	2.5652e-5	9.2739e-7	6.986

one to use relatively coarse meshes to achieve high accuracy compared to low order methods. For Neumann boundary conditions, some errors seem to accumulate from the curved boundaries. This could arise from nearly inverted elements or suboptimal performance of the linear solver.

Table 4.6: Table of convergence for three dimensional Neumann Problem with curved test functions.

	#DOFs	6458	25,084	100,772	Convergence Rate
GLPBF Deg.	Quadratic	2.54e-1	9.18e-3	5.19e-3	1.229
	Cubic	3.08e-1	1.14e-1	2.19e-2	2.119
	Quartic	3.96e-3	3.56e-4	5.03e-5	4.77
	Quintic	2.52e-3	3.63e-4	6.81e-5	3.95
	Sextic	8.03e-3	1.90e-3	8.30e-5	4.99

Chapter 5

Direct Treatment of Neumann Boundary Conditions with Boundary Integrals

In the traditional derivation of the weak form, Neumann boundary conditions arise naturally from the integration by parts of the PDE multiplied by its test function. These *natural boundary conditions* can then be assembled into the load vector as an additional surface term to the computed volume terms in the stiffness matrix and boundary term of the load vector. In the method of weighted residual formulation, natural boundary conditions may be enforced in several ways. The first is to take an appropriate choice of test function which is smooth at the boundary and applying integration by parts to the resulting integral, hence the term *natural* boundary conditions [24]. This

manner is the most common used in finite element methods, because it often results in a symmetric positive definite linear system for elliptic equations.

Because of the volumetric nature of the test functions, this requires a volume integral to be computed. There are two factors which make complicate the implementation of methods. First, the use of high order volumetric elements requires a well-defined mapping that blends the curved boundary with the interior of several elements. Constructing this mapping is possible as in [59, 60] or as outlined in Section 4.1, but it is difficult to determine *a priori* if the resulting elements are well-conditioned and have nonzero Jacobian everywhere. In particular, if the parameterization of the curve has a very large curvature, then it is possible for the parametric mappings given in Section 4.1 to be inverted in physical space. Second, is that the continuity requirements of the test functions require an isoparametric or superparametric mapping over a curved element, which in general are not polynomials. This leads to variational crimes in the choice of numerical quadrature that only work for polynomials defined on the reference element [66].

However for collocation methods such as finite difference methods, test functions are chosen to be Dirac delta functions, which do not satisfy the smoothness requirements for integration by parts. In practice, Neumann boundary conditions may be enforced directly at the boundary point. However, this becomes difficult when the unit normal of the surface Γ is not defined at features such as corners or ridges. If one has two or more different boundary conditions meeting at a single point, then it is no longer clear how

to satisfy all boundary conditions at the same time. This situation can be avoided if the Dirac delta function is replaced with a new test function that can be integrated over the boundary of the mesh, since the normal vector could be defined almost everywhere on the boundary.

Therefore, it would be preferable to avoid the definition of new volumetric elements at all costs while still maintaining the advantages of the treatment of Neumann boundary conditions on the surface of the mesh. Therefore, we propose to incorporate the integration of Neumann boundary conditions along the boundary alone. This can be interpreted as a new type of test function whose support is contained only within the boundary of the domain, effectively solving

$$\int_\Gamma \frac{\partial u}{\partial n} v \, \mathrm{d}\Gamma = \int_\Gamma g v \, \mathrm{d}\Gamma, \tag{5.1}$$

where v is the trace of a finite element test function defined over the volume of the mesh.

Theorem 5. *Let $v : \Gamma \to \mathbb{R}$ be a test function defined on Γ with compact support, and solution u to the strong form of the Laplace equation. Then, for any function $w \in \{w' \in H^1(\Omega) : w'|_\Gamma = v\}$, (5.1) is equivalent to the weak form with test function w,*

$$\int_\Omega \nabla u \cdot \nabla w \, \mathrm{d}\Omega = \int_\Omega f w \, \mathrm{d}\Omega + \int_\Gamma g w \, \mathrm{d}\Gamma.$$

.

Proof. From the Neumann boundary conditions and divergence theorem, one has

$$\begin{aligned}\int_\Gamma gv \ \mathrm{d}\Gamma &= \int_\Gamma \frac{\partial u}{\partial n} v \ \mathrm{d}\Gamma \\ &= \int_\Omega \nabla \cdot (w \nabla u) \ \ \mathrm{d}\Omega \\ &= \int_\Omega \nabla u \cdot \nabla w \ \mathrm{d}\Omega + \int_\Omega w \Delta u \ \mathrm{d}\Omega.\end{aligned}$$

Substituting $-\Delta u = f$ and subtracting that term from both sides gives the weak formulation with test function w. □

Theorem 5 allows one to treat the Neumann boundary conditions directly on the surface in a manner that is directly equivalent to the traditional weak formulation using test functions defined over the volume of the domain. As the surface can be more easily parameterized than volume elements generated from Section 4.1, this approach has a significant advantage. Furthermore, (5.1) allows for the natural boundary conditions to be enforced over features where no normal may be defined pointwise.

Similarly, estimation of normal derivatives can either be taken from a pre-existing CAD model or exact geometry or they can be computed using the WALF-reconstructed surface. The stiffness matrix is now contained inside the term

$$\int_\Gamma \frac{\partial u}{\partial n} v \ \mathrm{d}\Gamma = \int_\Gamma (v \nabla u) \cdot \boldsymbol{n} \ \mathrm{d}\Gamma. \tag{5.2}$$

The computation of (5.2) is performed in the same manner as outlined in

Section 4.3 through the use of numerical quadrature rules and estimates of the weighted area.

The treatment of Neumann boundary conditions described above is agnostic of the test functions used inside of the interior. For AES-FEM, finite element test functions are taken from the mesh. However, these test functions could be other types of functions with compact support such as radial-basis functions or even Dirac delta functions. In the latter case, this corresponds with GFD. To the author's knowledge, this is the first treatment of Neumann boundary conditions in such manner for finite difference methods. This is particularly attractive for GFD methods because Neumann boundary conditions are generally treated only at a single point as opposed to some nonzero measure set. This can be ambiguous for many geometries where a normal may not even be defined at points which lie on features such as ridges or corners. Because the boundary has a well-defined piecewise continuous normal vector for most applications, integration can be performed over the geometry.

Theorem 6. *Let u be a smooth function $C^{d+1}(\Omega) \cap C^0\left(\overline{\Omega}\right)$, and let u_h be a degree d polynomial approximation of the solution u to $O\left(h^{d+1}\right)$. Assume that the boundary Γ is represented exactly, and that $v \in L^1_{\text{loc}}(\Gamma)$. Then*

$$\left| \int_\Gamma v \frac{\partial (u - u_h)}{\partial n} \mathrm{d}\Gamma \right| \leq C(v) h^d. \tag{5.3}$$

Proof. The weighted residual of the normal derivative error can be bounded

by

$$\left| \int_{\Gamma} v \frac{\partial \left(u - u_h \right)}{\partial n} \mathrm{d}\Gamma \right| \leq \int_{\Gamma} |v| \left| \frac{\partial \left(u - u_h \right)}{\partial n} \right| \mathrm{d}\Gamma. \tag{5.4}$$

By Holder's inequality, the normal derivative is bounded by 1-norm of the gradient vector,

$$\left| \frac{\partial \left(u - u_h \right)}{\partial n} \right| = \left| \nabla \left(u - u_h \right) \cdot \boldsymbol{n} \right| \leq \| \nabla \left(u - u_h \right) \|_1 \| \boldsymbol{n} \|_{\infty} \leq \| \nabla \left(u - u_h \right) \|_1 \tag{5.5}$$

because $\boldsymbol{n}$ is the unit vector normal to Γ. Taylor's theorem and the assumption that u is smooth implies that for each first order partial derivative there exists a constant $C_i > 0$ such that

$$\left| \frac{\partial}{\partial x_i} \left(u - u_h \right) \right| \leq C_i h^d. \tag{5.6}$$

Combining (5.5) and (5.6) for each partial derivative and substituting into the right hand side of (5.4) then gives

$$\left| \int_{\Gamma} v \frac{\partial \left(u - u_h \right)}{\partial n} \mathrm{d}\Gamma \right| \leq C \left(v \right) h^d,$$

where $C \left(v \right) = \int_{\Gamma} |v| \, \mathrm{d}\Gamma \left(\sum_{i=1}^{d} C_i \right)$. □

Theorem 6 allows for the explicit approximation of Neumann boundary conditions up to sufficiently high-order approximations. Furthermore, it couples the interplay of internal and external forces because the gradient term ∇u will be approximated by vertices residing on the interior of the domain

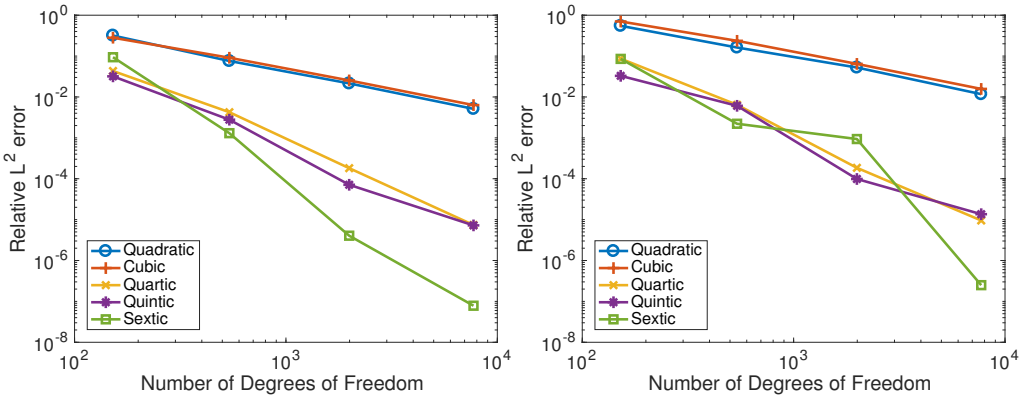

Figure 5.1: Convergence plot of GFD with Neumann boundary treatment.

and not just along the boundary.

To test the accuracy of the new enforcement of Neumann boundary conditions, we again solve Poisson equation on a square domain with a circular hole as described in Section 4.4. The solution to the problem is given by (4.11), and both Dirichlet and Neumann boundary conditions are implemented on the interior hole. The PDE is discretized using generalized finite differences for vertices on the interior, and the Neumann boundary conditions are discretized as (5.1). Dirichlet boundary conditions are computed by directly substituting the function value at Dirichlet nodes directly into the finite difference rule and subtracting them from the load vector.

Figure 5.1 shows the convergence of the GFD method for both Dirichlet and Neumann boundary conditions. Table 5.1 shows that the Dirichlet problem converges at a high order even though the curved boundary is not represented in the discretization. The Neumann problem also converges to high order, as shown in Table 5.2, with slightly larger errors than the cor-

Table 5.1: Relative errors for Dirichlet boundary conditions with GFD.

	#DOFs	152	540	1992	7716	Convergence Rate
GLPBF Deg.	Quadratic	3.18e-1	7.60e-2	2.15e-2	5.12e-3	2.10
	Cubic	2.81e-1	9.11e-2	2.54e-2	6.32e-3	1.93
	Quartic	4.31e-2	4.24e-3	1.81e-4	7.39e-6	4.42
	Quintic	3.19e-2	2.78e-3	7.12e-5	7.23e-6	4.27
	Sextic	9.38e-2	1.30e-3	4.04e-6	7.84e-8	7.13

Table 5.2: Relative errors for GFD with Neumann boundary conditions implemented on the surface.

	#DOFs	152	540	1992	7716	Convergence
GLPBF Deg.	Quadratic	5.50e-1	1.62e-1	5.25e-2	1.17e-2	1.96
	Cubic	7.02e-1	2.36e-1	6.44e-2	1.57e-2	1.93
	Quartic	8.68e-2	6.43e-3	1.85e-4	9.53e-6	4.64
	Quintic	3.29e-2	6.08e-3	9.86e-5	9.58e-6	3.97
	Sextic	8.54e-2	2.21e-3	9.36e-4	2.50e-7	6.49

responding mesh with Dirichlet boundary conditions. It should be noted that for degree d polynomials the consistency error should be dominated by the GFD approximation in the interior where second derivatives are taken, which only lead to $O\left(h^{d-1}\right)$ instead of the $O\left(h^{d}\right)$ consistency error of the Neumann boundary condition given by Theorem 6. Therefore, the results for odd degree polynomials are optimal while even degree polynomials enjoy an extra order of convergencek.

Chapter 6

Application: Linear Elasticity

Linear elasticity in solid mechanics is a common application for FEM due to the ease of imposition of a diverse set of material properties, boundary conditions on complex geometries. Indeed, FEM software makes up a one billion dollar industry and is a crucial part of the automotive, aerospace, and shipbuilding industries [31]. Here we compare the new superparametric test functions AES-FEM from Chapter 4 with the GFD with the alternative Neumann boundary condition treatment from Chapter 5 to the solution of the equations of linear elasticity on problems with curved geometries.

Linear elasticity, and more generally the field of solid mechanics, is an excellent application for comparing finite element methods because the development of FEMs has long been motivated by the solid mechanics community. Even the nomenclature of *stiffness matrix* and *load vector* have their roots in solid mechanics where they represent the internal stresses of a mechanical

object counteracting the external loads applied to it.

Consider an elastic body $\Omega \subset \mathbb{R}^3$ with so-called material coordinate given by the vector $\boldsymbol{x} \in \mathbb{R}^3$. The elastic body may be in a deformed configuration Ω' where each material coordinate has a new position $\boldsymbol{x}' = \boldsymbol{x} + \boldsymbol{u}$, with $\boldsymbol{u} = \boldsymbol{u}(\boldsymbol{x})$ being the displacement of the material coordinate $\boldsymbol{x}$. The deformation tensor of the material is the Jacobian of the material

$$(\nabla \boldsymbol{u})_{ij} = \frac{\partial u_i}{\partial x_j}, \tag{6.1}$$

from which the components of the symmetric rank two linear strain tensor $\boldsymbol{e}$ is given by

$$e_{ij} = \frac{1}{2}\left(\frac{\partial u_i}{\partial x_j} + \frac{\partial u_j}{\partial x_i}\right). \tag{6.2}$$

The linear strain tensor may also be represented in Voigt notation [74] using the 6-vector

$$\boldsymbol{e} = \left[e_1, e_2, e_3, 2e_{23}, 2e_{13}, 2e_{12}\right]^T. \tag{6.3}$$

The description of the material is given in the form of certain material parameters, of which we assume knowledge of either the Young's modulus (E) and the Poisson ratio (ν) or the Lamé parameters,

$$\lambda = \frac{E\nu}{(1-2\nu)(1+\nu)}$$
$$\mu = \frac{E}{2(1+\nu)}.$$

The internal stresses of the material are given by the symmetric rank two Cauchy strain tensor, $\boldsymbol{\sigma} = \sigma_{ij}$, which may be expressed in Voigt notation using the 6-vector

$$\boldsymbol{\sigma} = \left[\sigma_{11}, \sigma_{22}, \sigma_{33}, \sigma_{23}, \sigma_{13}, \sigma_{12}\right]^T. \tag{6.4}$$

The components of the stress and strain tensors are related by the constitutional equations. For homogeneous materials, the components of the rank four stiffness tensor are given in terms of the Lamé parameters as

$$\sigma_{ij} = C_{ijrs} e_{rs} = \left(\lambda \delta_{ij} \delta_{rs} + 2\mu \delta_{ir} \delta_{js}\right) e_{rs}, \tag{6.5}$$

which satisfy the symmetries $C_{ijrs} = C_{rsij}$ and $C_{ijrs} = C_{jirs}$. The stiffness tensor may be represented in Voigt notation as a symmetric square matrix

$$\boldsymbol{C} = \begin{bmatrix} \lambda + 2\mu & \lambda & \lambda & 0 & 0 & 0 \\ \lambda & \lambda + 2\mu & \lambda & 0 & 0 & 0 \\ \lambda & \lambda & \lambda + 2\mu & 0 & 0 & 0 \\ 0 & 0 & 0 & \mu & 0 & 0 \\ 0 & 0 & 0 & 0 & \mu & 0 \\ 0 & 0 & 0 & 0 & 0 & \mu \end{bmatrix}. \tag{6.6}$$

The balance of internal forces experienced by the material points of Ω is

given by the equations

$$\nabla \cdot \boldsymbol{\sigma}^T + \boldsymbol{f} = \mathbf{0} \qquad \text{for } \boldsymbol{x} \in \Omega \tag{6.7}$$

where $\boldsymbol{f} = \boldsymbol{f}(\boldsymbol{x})$ is the body forces experienced at the material coordinate $\boldsymbol{x}$. Boundary conditions may be imposed on the boundary of the domain, $\partial\Omega$, in one of two ways. A subset of the boundary of the domain $\Gamma_N \subset \partial\Omega$ may experience external tractions $\boldsymbol{t}$ which are defined by

$$\boldsymbol{\sigma} \cdot \boldsymbol{n} = \boldsymbol{t} \qquad \text{for } \boldsymbol{x} \in \Gamma_N, \tag{6.8}$$

where $\boldsymbol{n}$ is the unit outer normal vector of the domain. Another subset $\Gamma_D \subset \partial\Omega$ may have prescribed displacement conditions in the form of

$$\boldsymbol{D}\boldsymbol{u}|_{\Gamma_D} = \boldsymbol{d} \qquad \text{for } \boldsymbol{x} \in \Gamma_D, \tag{6.9}$$

where $\boldsymbol{D} \in \mathbb{R}^{m\times 3}$, $m \leq 3$ determines whether the material point is fixed $m = 3$ or has "sliding" boundary conditions along a line or a plane.[1]

Multiplying (6.7) by a test function $\delta\boldsymbol{u}$ (also known as a virtual displacement [74]) which satisfies $\delta\boldsymbol{u}|_{\Gamma_D} = \mathbf{0}$ and performing integration by parts

[1]For the purposes of this dissertation, we assume that the matrix $\boldsymbol{D}$ is fixed. However, FEM software usually allows for boundary conditions where material points may slide tangent to the suface, in which case $\boldsymbol{D} = \boldsymbol{n}^T$.

over Ω leads to the principle of virtual work

$$\int_{\Omega} \boldsymbol{\sigma} : \delta \boldsymbol{e} \, \mathrm{d}\Omega = \int_{\Omega} \boldsymbol{f} \cdot \delta \boldsymbol{u} \, \mathrm{d}\Omega + \int_{\Gamma_N} \boldsymbol{t} \cdot \delta \boldsymbol{u} \, \mathrm{d}\Gamma, \tag{6.10}$$

where $\boldsymbol{\sigma} : \delta \boldsymbol{e} = \sum_{i,j} \sigma_{ij} \delta e_{ij}$ and $\boldsymbol{f} \cdot \delta \boldsymbol{e} = \sum_i f_i \delta u_i$. All versions of FEM determine a solution by solving (6.10). Substituting the constitutional equations (6.5) into (6.12) gives the principle of virtual work in terms of the material displacements

$$\int_{\Omega} (\boldsymbol{C}\boldsymbol{e}) : \delta \boldsymbol{e} \, \mathrm{d}\Omega = \int_{\Omega} \boldsymbol{f} \cdot \delta \boldsymbol{u} \, \mathrm{d}\Omega + \int_{\Gamma_N} \boldsymbol{t} \cdot \delta \boldsymbol{u} \, \mathrm{d}\Gamma. \tag{6.11}$$

Using the finite element discretization, a linear system of equations may be constructed from (6.11)

$$\boldsymbol{A}\boldsymbol{u} = \boldsymbol{b}, \tag{6.12}$$

where $\boldsymbol{A}$ is the stiffness matrix and $\boldsymbol{b}$ is the load vector. The assembly of (6.12) in AES-FEM is similar to traditional FEM matrix assembly procedures.

6.1 Infinite Plate with Circular Hole

The following problem is from [68], where an infinite thin plate with a circular hole of radius a is applied with unit traction in the $+x$-direction at the point at infinity as shown in Figure 6.1. The analytic solution of the components

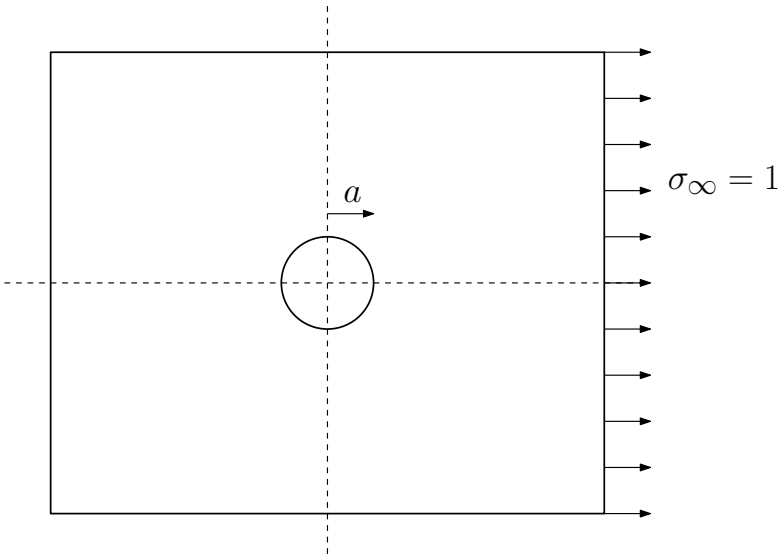

Figure 6.1: Geometry of the infinite thin plate with circular hole. Lines of symmetry along the x- and y-axes are denoted by the dashed lines.

of the Cartesian stresses is given in polar coordinates as [5]

$$\sigma_{xx} = 1 - \frac{a^2}{r^2}\left(\frac{3}{2}\cos(2\theta) + \cos(4\theta)\right) + \frac{3a^4}{2r^4}\cos(4\theta) \tag{6.13}$$

$$\sigma_{yy} = -\frac{a^2}{r^2}\left(\frac{1}{2}\cos(2\theta) - \cos(4\theta)\right) - \frac{3a^4}{2r^4}\cos(4\theta) \tag{6.14}$$

$$\sigma_{xy} = -\frac{a^2}{r^2}\left(\frac{1}{2}\sin(2\theta) + \sin(4\theta)\right) + \frac{3a^4}{2r^4}\sin(4\theta)\,. \tag{6.15}$$

The problem is solved on a finite portion of the upper-right quadrant with length $L = 1$ and an inner hole radius of $a = 0.25$ as shown in Figure 6.2. The external tractions on the boundary are computed at the boundary using as $\boldsymbol{t} = \boldsymbol{\sigma}\boldsymbol{n}$, with the entries of σ_{ij} computed using given by (6.13) through (6.15). It should also be noted that the equations above give the external

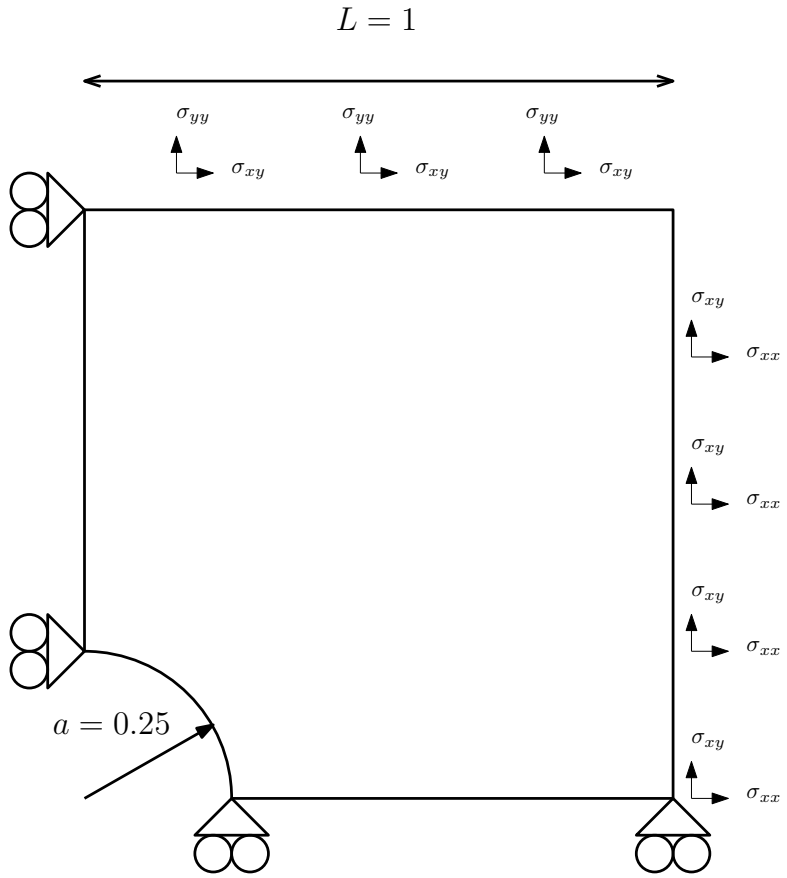

Figure 6.2: Set up of quadrant for numerical experiment. Boundary tractions are enforced from the analytical expressions for the stress tensor, and sliding boundary conditions are imposed on the $+x$- and $+y$-axes.

tractions on the the hole as $\boldsymbol{t} = \mathbf{0}$. Sliding boundary displacement conditions are enforced along the lines of symmetry by directly imposing the conditions $\boldsymbol{u} \cdot \boldsymbol{n} = 0$ on the $+x$- and $+y$-axes.

This benchmark is noteworthy because it demonstrates that holes within otherwise ideal material can lead to a concentration of stresses near the hole. As the material around the hole deforms, the internal stresses tangential to the hole reach a maximum value of exactly $\sigma_{\max} = 3\sigma_\infty$ at the points $(0, \pm a)$. The factor of three is known as the *stress concentration factor* in mechanical engineering literature, and is defined as

$$K = \frac{\sigma_{\max}}{\sigma_\infty}. \tag{6.16}$$

If the internal stresses accumulate past a certain material-dependent threshold, then cracks are more likely to nucleate and propagate from the high stress regions. Figure 6.3 shows the deformation of the finite region of plate along with the $\sigma_{\theta\theta}$ component of the stress tensor, often called the *hoop stresses*, for a mesh with approximately 4000 degrees of freedom. The material parameters chosen were a Young's modulus of 200 GPa and Poisson ratio of 0.3, which are approximately the material parameters of steel. The value of $\sigma_\infty = 20$ GPa, and the results shows good agreement with the analytic solution which predicts a maximum of 60 GPa at the top of the circle and -20 GPa at the .

We study the convergence of this problem for a sequence of meshes for

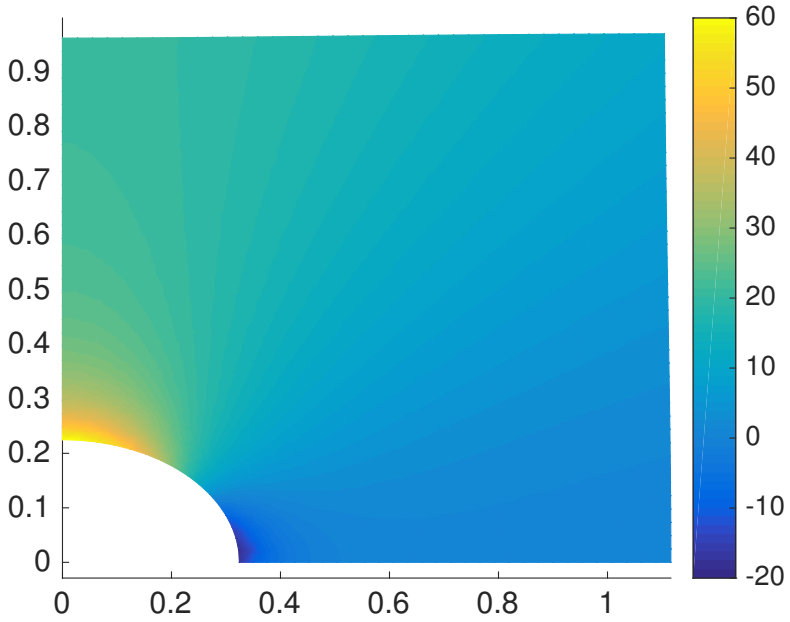

Figure 6.3: Distribution of stresses on the deformed configuration of the computational domain from Figure 6.2.

the above problem. The linear finite element meshes are generated by Gmsh [29], from which the curved superparametric elements are constructed adjacent to the circular hole as described in Section 4.1. The resulting linear systems were solved using the preconditioned GMRES solver in Matlab® to a tolerance of 10^{-8} with incomplete LU-factorization as a preconditioner. Figure 6.4 shows the convergence of AES-FEM for quadratic, quartic, and sextic GLPBFs using for both linear and superparametric test functions. As can be seen, there is significant advantage using high order basis functions with superparametric test functions. For linear test functions, the rate of convergence is significantly reduced for high degree basis functions due to the accumulation of geometric errors near the circular hole. However, these

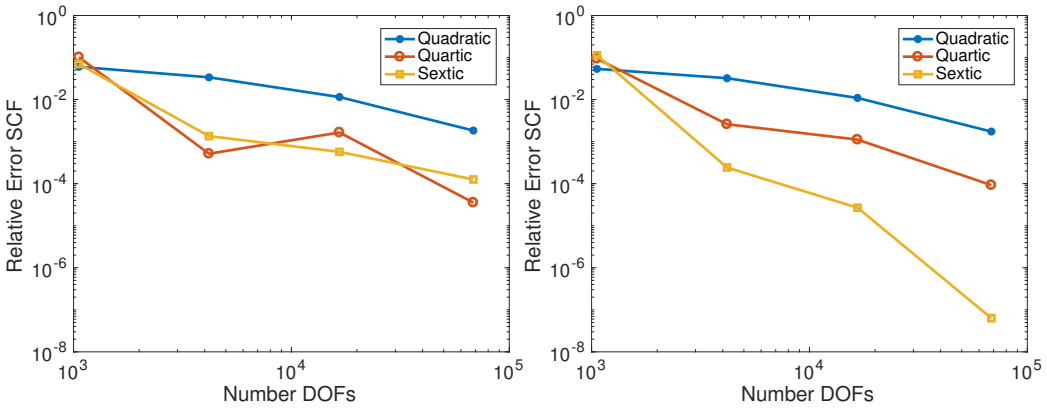

Figure 6.4: Convergence of stress concentration error for AES-FEM with linear (left) superparametric (right) test functions on the boundary.

geometric errors are significantly reduced when using superparametric elements which are able to approximate the curvature of the hole to high order. It can be noted that the stress concentration factor can be estimated reliably to below 10^{-7} with less than 30,000 degrees of freedom when using degree six polynomials with curved elements.

6.2 Thick-Walled Annulus

Now we consider another common benchmark in linear elasticity as outlined in [68]. The domain is a thick-walled annulus with outer radius a and inner radius b shown in Figure 6.5. Uniform pressure may be imposed on the inner and outer surfaces of the annulus measuring P_i and P_o, respectively. Under the assumption of rotational symmetry, the displacements are assumed to

only be in the radial direction and may written as

$$u_r = C_1 r + \frac{C_2}{r}, \tag{6.17}$$

where

$$C_1 = \frac{1-\nu}{E}\ \frac{b^2 P_i - a^2 P_o}{a^2 - b^2},$$
$$C_2 = \frac{1-\nu}{E}\ \frac{a^2 b^2 \left(P_i - P_o\right)}{a^2 - b^2};$$

while the stress tensor has only two nonzero components

$$\sigma_{rr} = \frac{E}{(1-\nu^2)}\left[(1+\nu)\, C_1 - \frac{1-\nu}{r^2} C_2\right], \tag{6.18}$$
$$\sigma_{\theta\theta} = \frac{E}{(1-\nu^2)}\left[(1+\nu)\, C_1 + \frac{1-\nu}{r^2} C_2\right], \tag{6.19}$$

where E represents the Young's modulus of the material and ν is the Poisson ratio.

The computational domain is chosen to be the first quadrant of the anulus, with sliding boundary conditions applied to the $+x$- and $+y$-axes. The degrees of freedom corresponding to these degrees of freedom are omitted from the global stiffness matrix and assembled into the load vector. Natural boundary conditions at the inner and outer arcs are imposed as surface tractions

$$\boldsymbol{t} = P\hat{\boldsymbol{n}},$$

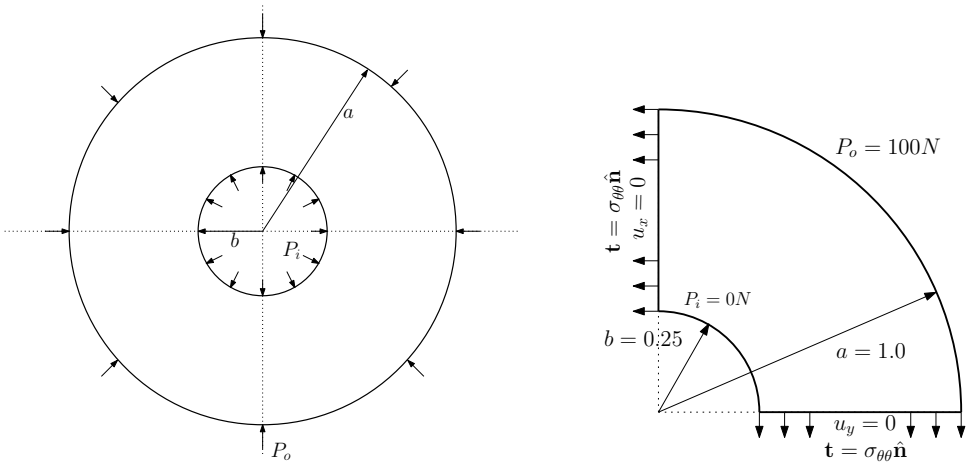

Figure 6.5: A thick walled annulus with external loading and lines of symmetry (left), and the computational domain used in the numerical experiments (right).

where $\hat{\boldsymbol{n}}$ is the unit normal of the surface oriented outwards and P is the corresponding value of pressure. In our numerical experiments, we use the value of $P_i = 0$ GPa and $P_o = 100$ GPa. The x and y axes also have surface tractions applied to them taken from the analytic solution from (6.19). We choose material parameters $E = 200$ GPa and $\nu = 0.3$ for the convergence study. The results of the convergence study are presented in Figure 6.6. Again, the results indicate that high order representation of the geometry is required to guarantee high order convergence.

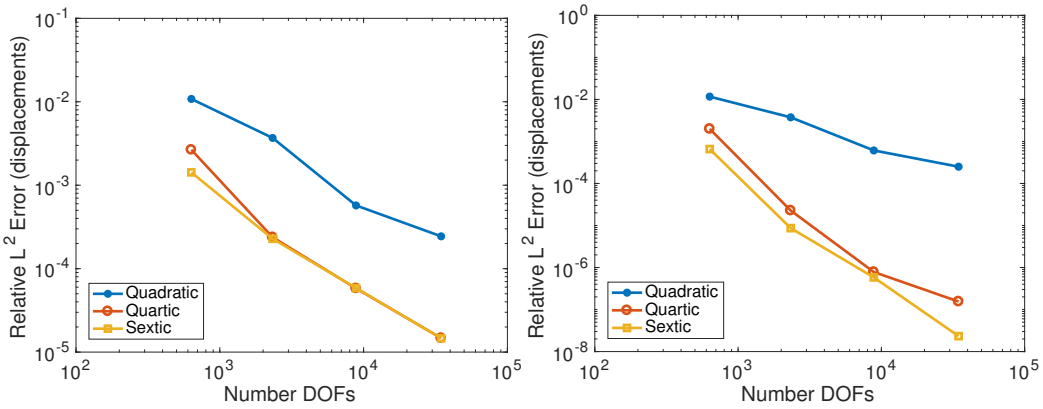

Figure 6.6: Convergence of AES-FEM for thick-walled annulus using linear (left) and superparametric test functions (right).

Chapter 7

Conclusion

In this dissertation, adaptive extended stencil finite element method was improved to account for elliptic PDEs with Neumann boundary conditions on curved geometries. This was achieved by using superparametric elements which can be created from an analytic representation of the geometry or by using high order surface reconstruction techniques such as WALF. The superparametric test functions improve the consistency of the weak formulation by minimizing geometric errors which restrict the order of accuracy for problems with Neumann boundary conditions in curved geometries. Additionally, these superparametric elements are only constructed when they are adjacent to the boundary, which reduces the total computational work load overall. Therefore, using a high degree polynomial basis with curved superparametric elements can result in significantly higher accuracy with less degrees of freedom than low order methods.

This dissertation also proposes a new method for incorporating Neumann boundary conditions for methods of weighted residuals such as generalized finite difference methods. This is achieved by designing new test functions defined only on the boundary of the domain and computing a weighted residual of the Neumann boundary conditions on the boundary of the domain. This new computation of the Neumann boundary conditions is advantageous over the existing pointwise implementation of Neumann boundary conditions for finite difference methods because it allows for these conditions to be computed points which have no well defined normal direction.

Lastly, we showed that AES-FEM can be used for problems in linear elasticity for problems with Neumann boundary conditions, curved geometries, and non-smooth boundaries. We were able to show that AES-FEM can achieve high order convergence for many classical benchmark problems in linear elasticity when superparametric elements were used to represent the boundary. These superparametric elements are necessary to ensure that AES-FEM can achieve high order convergence for curved geometries.

AES-FEM has several directions for further research. Although this dissertation has focused on elliptic problems, AES-FEM can be easily used in solving time-dependent equations. It would be of interest to use AES-FEM in Adaptive Lagrangian-Eulerian (ALE) methods and other time dependent problems with moving geometry. These would require specialized treatment of the test functions so as to prevent folding under large deformations. Investigation into parallelizing AES-FEM

Additionally, the direct treatment of Neumann boundary conditions presented in Chapter 5 can be used to combine generalized finite difference discretizations with problems involving sharp features in novel manner.

Bibliography

[1] I. Babuska and A. K. Aziz, *On the angle condition in the finite element method*, SIAM Journal on Numerical Analysis, 13 (1976), pp. pp. 214–226.

[2] I. Babuska, U. Banerjee, and J. Osborn, *Survey of meshless and generalized finite element methods: a unified approach.*, Acta Numerica, (2003), pp. 1–125.

[3] F. Bassi and S. Rebay, *High-order accurate discontinuous finite element solution of the 2D euler equations*, Journal of Computational Physics, 138 (1997), pp. 251–285.

[4] Y. Bazilevs, V. Calo, J. Cottrell, J. Evans, T. Hughes, S. Lipton, M. Scott, and T. Sederberg, *Isogeometric analysis using t-splines*, Computer Methods in Applied Mechanics and Engineering, 199 (2010), pp. 229–263.

[5] T. Belytschko, Y. Krongauz, J. Dolbow, and C. Gerlach, *On the completeness of meshfree particle methods*, Int. J. Numer. Meth. Engrg., 45 (1998), pp. 785–819.

[6] T. Belytschko, Y. Krongauz, D. Organ, M. Fleming, and P. Krysl, *Meshless methods: An overview and recent developments*, Comput. Methods Appl. Mech. Engrg., 139 (1996), pp. 3–47.

[7] T. Belytschko, Y. Y. Lu, and L. Gu, *Element-free Galerkin methods*, Int. J. Numer. Meth. Engrg., 37, pp. 229–256.

[8] J. J. Benito, F. Ureña, and L. Gavete, *The generalized finite difference method*, in Leading-Edge Applied Mathematical Modeling Research, M. P. Álvarez, ed., Nova Science Publishers, Inc., 2008, ch. 7.

[9] M. Berger, *Adaptive finite difference methods in fluid dynamics*, in von Karman Lecture Notes on CFD, 1987. NYU/DOE report 03077-277.

[10] S. C. Brenner and R. Scott, *The Mathematical Theory of Finite Element Methods*, vol. 15, Springer Science & Business Media, New York, 2008.

[11] M. Buhmann, *Radial basis functions: theory and implementations*, Cambridge University Press, Cambridge, 2003.

[12] T. F. Chan, *Rank revealing {QR} factorizations*, Linear Algebra and its Applications, 88?89 (1987), pp. 67 – 82.

[13] K. C. Chung, *A generalized finite-difference method for heat transfer problems of irregular geometries*, Numerical Heat Transfer, 4 (1981), pp. 345–357.

[14] P. G. Ciarlet, *The Finite Element Method for Elliptic Problems*, Society for Industrial and Applied Mathematics, 2002.

[15] B. Clark, *Accurate, Semi-Implicit Methods with Mesh Adaptivity for Mean Curvature Flow and Surface Diffusion Using Triangulated Surfaces*, PhD thesis, Stony Brook University, 2012.

[16] B. Clark, N. Ray, and X. Jiao, *Surface mesh optimization, adaption, and untangling with high-order accuracy*, in Proceedings of 21st International Meshing Roundtable, San Jose, CA, 2012.

[17] E. Cohen, T. Martin, R. M. Kirby, T. Lyche, and R. F. Riesenfield, *Analysis-aware modeling: Understanding quality considerations in modeling for isogeometric analysis*, Computer Methods in Applied Mechanics and Engineering, 199 (2010).

[18] R. Conley, *Overcoming Element Quality Dependence of Finite Element Methods*, PhD thesis, State University of New York at Stony Brook, 2016.

[19] R. Conley, T. J. Delaney, and X. Jiao, *Overcoming element quality dependence of finite elements with adaptive extended stencil FEM (AES-FEM)*, Int. J. Num. Method. Engrg., 108 (2016), pp. 1054–1085.

[20] J. A. Cottrell, T. J. R. Hughes, and Y. Bazilevs, *Isogeometric Analysis: Toward Integration of CAD and FEA*, Wiley, Chichester, West Sussex, UK, 2009.

[21] J. A. Cottrell, A. Reali, Y. Bazilevs, and T. J. R. Hughes, *Isogeometric analysis of structural vibrations*, Comput. Meth. Appl. Mech. Engrg., 195 (2006), pp. 5257–5296.

[22] M. Crouzeix and P.-A. Raviart, *Conforming and nonconforming finite element methods for solving the stationary stokes equations i*, ESAIM: Mathematical Modelling and Numerical Analysis - Modélisation Mathématique et Analyse Numérique, 7 (1973), pp. 33–75.

[23] H. Fahs, *Improving accuracy of high-order discontinuous Galerkin method for time-domain electromagnetics on curvilinear domains*, International Journal of Computational Mathematics, 88 (2011), pp. 2124–2153.

[24] B. A. Finlayson, *The Method of Weighted Residuals and Variational Principles*, Academic Press, New York, 1973.

[25] B. Fornberg, *Calculation of weights in finite difference formulas*, SIAM Review, 40 (1998), pp. 685–691.

[26] K. P. S. Gahalaut, *Isogeometric Analysis: Condition Number Estimates and Fast Solvers*, PhD thesis, Johannes Kepler Universit at, 2013.

[27] A. Gargallo-Peiró, X. Roca, J. Peraire, and J. Sarrate, *Defining quality measures for validation and generation of high-order tetrahedral meshes*, in Proceedings of the 22nd International Meshing Roundtable, Springer International Publishing, 2014, pp. 109–126.

[28] L. Gavete, M. Gavete, and J. Benito, *Improvements of generalized finite difference method and comparison with other meshless methods*, Appl. Math. Model., 27 (2003), pp. 831–847.

[29] C. Geuzaine and J.-F. Remacle, *Gmsh: a three-dimensional finite element mesh generator with built-in pre- and post-processing facilities*, Int. J. Numer. Meth. Engrg., 79 (2009), pp. 1309–1331.

[30] R. Gingold and J. Monaghan, *Smoothed particle hydrodynamics: theory and application to non-spherical stars*, Mon. Not. R. Astron. Soc., 181 (1977), pp. 375–89.

[31] T. J. Hughes, J. A. Cottrell, and Y. Bazilevs, *Isogeometric analysis: CAD, finite elements, NURBS, exact geometry and mesh refinement*, Comput. Meth. Appl. Mech. Engrg., 194 (2005), pp. 4135–4195.

[32] T. J. R. Hughes, J. A. Cottrell, and Y. Bazilevs, *Isogeometric analysis: CAD, finite elements, NURBS, exact geometry and mesh refinement*, Comput. Meth. Appl. Mech. Engrg., 194 (2005), pp. 4135–4195.

[33] P. Jensen, *A finite difference technique for variable grids*, in Conference on Computer Oriented Analysis of Shell Structures, Palo Alto, CA., Aug. 1970.

[34] P. S. Jensen, *Finite difference techniques for variable grids*, Comput. Struct., 2 (1972), pp. 17–29.

[35] X. Jiao and D. Wang, *Reconstructing High-Order Surfaces for Meshing*, in Proceedings of the 19th International Meshing Roundtable, S. Shontz, ed., Springer Berlin Heidelberg, 2010, pp. 143–160.

[36] X. Jiao and D. Wang, *Reconstructing high-order surfaces for meshing*, Engineering with Computers, 28 (2012), pp. 361–373.

[37] X. Jiao and H. Zha, *Consistent computation of first-and second-order differential quantities for surface meshes*, in ACM Symposium on Solid and Physical Modeling, Stony Brook, NY, 2008, ACM, pp. 159–170.

[38] A. Johnen, J.-F. Remacle, and C. Geuzaine, *Geometrical validity of curvilinear finite elements*, J. Comput. Phys., 233 (2013), pp. 359 – 372.

[39] A. Johnen, J. F. Remacle, and C. Geuzaine., *Geometrical validity of curvilinear finite elements*, J. Comput. Phys., 233 (2013), pp. 359–372.

[40] P. Knupp, *Achieving finite element mesh quality via optimization of the jacobian matrix norm and associated quantities. part i: a framework*

for surface mesh optimization, Int. J. Numer. Meth. Engrg., 48 (2000), pp. 401–420.

[41] P. M. Knupp, *Algebraic mesh quality metrics*, SIAM J. Sci. Comput., 23 (2001), pp. 193–218.

[42] P. Lancaster and K. Salkauskas, *Surfaces generated by moving least squares methods*, Mathematics of Computation, 37 (1981), pp. 141–158.

[43] R. J. LeVeque, *Finite Difference Methods for Ordinary and Partial Differential Equations: Steady State and Time Dependent Problems*, SIAM, Philadelphia, 2007.

[44] S. Lipton, J. A. Evans, Y. Bazilevs, T. Elguedj, and T. J. R. Hughes, *Robustness of isogeometric structural discretizations under severe mesh distortion*, Computer Methods in Applied Mechanics and Engineering, 199 (2010).

[45] T. Liszka and J. Orkisz, *The finite difference method at arbitrary irregular grids and its application in applied mechanics*, Computers & Structures, 11 (1980), pp. 83 – 95. <ce:title>Special Issue-Computational Methods in Nonlinear Mechanics </ce:title>.

[46] T. Liszka and J. Orkisz, *The finite difference method at arbitrary irregular grids and its application in applied mechanics*, Comput. Struct., 11 (1980), pp. 83–95.

[47] L. B. Lucy, *A numerical approach to testing of the fission hypothesis*, Astronomical Journal, 82 (1977), pp. 1013–1024.

[48] S. Milewski, *Meshless finite difference method with higher order approximation applications in mechanics.*, Arch. Comput. Method. E., 19 (2012), pp. 1–49.

[49] B. Nayroles, G. Touzot, and P. Villon, *Generalizing the finite element method: diffuse approximation and diffuse elements*, Comput. Mech., 10 (1992), pp. 307–318.

[50] J. Orkisz, *Finite Difference Method (Part, III)*, Springer, Heidelberg, 1998.

[51] V. N. Parthasarathy, C. M. Graichen, and A. F. H. AF, *A comparison of tetrahedron quality measures*, Finite Elem. Anal. Des., 15 (1993), pp. 255–261.

[52] N. Perrone and R. Kao, *A general finite difference method for arbitrary meshes*, Comput. Struct., 5 (1975), pp. 45–57.

[53] P. A. Raviart and J. M. Thomas, *A mixed finite element method for 2-nd order elliptic problems*, Springer Berlin Heidelberg, Berlin, Heidelberg, 1977, pp. 292–315.

[54] N. Ray, *High-Order Surface Reconstruction and its Applications to Surface Integrals and Surface Remeshing*, PhD thesis, Stony Brook University, 2013.

[55] N. Ray, D. Wang, X. Jiao, and J. Glimm, *High-order numerical integration over discrete surfaces*, SIAM Journal on Numerical Analysis, 50 (2012), pp. 3061–3083.

[56] X. Roca, A. Gargallo-Peiró, and J. Sarrate, *Defining quality measures for high-order planar triangles and curved mesh generation*, in Proceedings of the 20th International Meshing Roundtable, Springer Berlin Heidelberg, 2012, pp. 365–383.

[57] X. Roca, A. Gargallo-Peiró, and J. Sarrate, *Defining Quality Measures for High-Order Planar Triangles and Curved Mesh Generation*, Springer Berlin Heidelberg, Berlin, Heidelberg, 2012, pp. 365–383.

[58] R. Sanders, *Finite difference techniques for nonlinear hyperbolic conservation laws*, in Proceedings of the 1983 Summer Seminar on Large-Scale Computations in Fluid Mechanics, American Mathematics Society, 1983.

[59] R. Sevilla, S. Fernández-Méndez, and A. Huerta, *NURBS-enhanced finite element method (NEFEM)*, International Journal for Numerical Methods in Engineering, 76 (2008), pp. 56–83.

[60] ——, *3D NURBS-enhanced finite element method (NEFEM)*, International Journal for Numerical Methods in Engineering, 88 (2011), pp. 103–125.

[61] J. R. Shewchuk, *Triangle: Engineering a 2D quality mesh generator and Delaunay triangulator*, in Applied Computational Geometry Towards Geometric Engineering, Springer, Philadelphia, 1996, pp. 203–222.

[62] J. R. Shewchuk, *What is a good linear finite element? interpolation, conditioning, anisotropy, and quality measures.* preprint, 2002.

[63] C. Shu, H. Ding, and N. Zhao, *Numerical comparison of least square-based finite-difference (lsfd) and radial basis function-based finite-difference (rbffd) methods*, Comput. Math. Appl., 51 (2006), pp. 1297–1310.

[64] H. Si, *TetGen, a quality tetrahedral mesh generator and three-dimensional Delaunay triangulator v1.4*, 2006.

[65] H. Si, *TetGen, a Delaunay-based quality tetrahedral mesh generator*, ACM Trans. Math. Software, 41 (2015), pp. 11:1 – 11:36.

[66] G. Strang, *Variational crimes in the finite element method*, in Mathematical foundations of the finite element method with applications to partial differential equations, Baltimore, MD, 1972, Academic Press, pp. 689–710.

[67] J. W. Thomas, *Numerical Partial Differential Equations: Finite Difference Methods*, Springer, 1995.

[68] S. P. Timoshenko and J. N. Goodier, *Theory of Elasticity*, McGraw-Hill, 3 ed., 1987.

[69] F. Ureña, E. Salete, J. J. Benito, and L. Gavete, *Solving third- and fourth-order partial differential equations using gfdm: application to solve problems of plates.*, International Journal of Computer Mathematics, 89 (2012), pp. 366 – 376.

[70] D. Wang, B. Clark, and X. Jiao, *An analysis and comparison of parameterization-based computation of differential quantities for discrete surfaces*, Comput. Aid. Geom. Des., 26 (2009), pp. 510–527.

[71] D. Wang, B. L. Clark, and X. Jiao, *An analysis and comparison of parameterization-based computation of differential quantities for discrete surfaces*, Comput. Aid. Geom. Des., 26 (2009), pp. 510–527.

[72] G. B. Wright and B. Fornberg, *Scattered node compact finite difference-type formulas generated from radial basis functions*, J. Comput. Phys., 212 (2006), pp. 99 – 123.

[73] Y. Zhang, Y. Bazilevs, S. G. C. Bajaj, and T. J. R. Hughes, *Patient-specific vascular NURBS modeling for isogeometric analysis of blood flow*, Comput. Meth. Appl. Mech. Engrg., 196 (2007), pp. 2943–2959.

[74] O. Zienkiewicz, R. Taylor, and J. Zhu, *The Finite Element Method: Its Basis and Fundamentals*, Butterworth-Heinemann, London, 2013.

[75] M. Zlámal, *On the finite element method*, Numerische Mathematik, 12 (1968), pp. 394–409.

[76] ——, *Curved elements in the finite element method II*, SIAM J. Numer. Anal., 11 (1974), pp. 347–362.